Simultaneous retrievals of biomass-burning aerosols and trace gases from the ultraviolet to near-infrared over northern Thailand during the 2019 pre-monsoon season

Ukkyo Jeong[1,2,3], Si-Chee Tsay[3], Nai-Yung Christina Hsu[3], David M. Giles[3,4], John W. Cooper[3,4], Jaehwa Lee[2,3], Robert J. Swap[3], Brent N. Holben[3], James J. Butler[3], Sheng-Hsiang Wang[5], Somporn Chantara[6], Hyunkee Hong[7], Donghee Kim[7], and Jhoon Kim[8]

[1]Division of Earth Environmental System Science, Major of Spatial Information Engineering, Pukyong National University, Busan, Republic of Korea
[2]Earth System Science Interdisciplinary Center, University of Maryland, College Park, MD, USA
[3]NASA Goddard Space Flight Center, Greenbelt, MD, USA
[4]Science Systems and Applications, Inc., Lanham, MD, USA
[5]Department of Atmospheric Sciences, National Central University, Taoyuan City, Taiwan
[6]Environmental Science Research Center, Faculty of Science, Chiang Mai University, Chiang Mai, Thailand
[7]National Institute of Environmental Research, Incheon, Republic of Korea
[8]Dept. of Atmospheric Sciences, Yonsei University, Seoul, Republic of Korea

Correspondence to: Ukkyo Jeong (ukkyo.jeong@pknu.ac.kr)

Abstract. With the advent of spaceborne instruments in a geostationary constellation, measuring high-spectral resolution ultraviolet–visible (UV–Vis) and selected near-/shortwave-infrared (NIR/SWIR) radiances can enable probing the lifecycle of key atmospheric trace gases and aerosols at higher temporal resolutions over the globe. The UV-Vis measurements are important for retrieving several key trace gases (e.g., O_3, SO_2, NO_2, HCHO) and particularly for deriving aerosol characteristics (e.g., aerosol absorption and vertical profile). This study examines the merit of simultaneous retrievals of trace gases and aerosols using a ground-based spectroradiometer covering the UV–NIR to monitor their physicochemical processes, and to obtain reliable aerosol information for various applications. During the 2019 pre-monsoon season over northern Thailand, we deployed a ground-based SMART–s (Spectral Measurements for Atmospheric Radiative Transfer–spectroradiometer) instrument, which is an extended-range Pandora with reliable radiometric calibration in 330–820 nm range, to retrieve remotely sensed chemical and aerosol properties for the first time near biomass-burning sources. The high spectral-resolution (~1.0 nm full-width-half-maximum with ~3.7× oversampling) of Sun and sky measurements from SMART–s provides several key trace gases (e.g., O_3, NO_2, and H_2O) as well as aerosol properties covering the UV where significant light-absorption occurs by the carbonaceous particles. During the measurement period, highly correlated total column amounts of NO_2 and aerosol optical thickness (τ_{aer}) retrieved from the SMART–s (correlation coefficient, R = 0.74) indicated their common emissions from biomass-burning events. The SMART-s retrievals of spectral single-scattering albedo (ω_0) of smoke aerosols showed an abrupt decrease in the UV, which is an important parameter dictating photochemical processes in the atmosphere. The values of ω_0 and column precipitable water vapor (H_2O) gradually increase with the mixing of biomass-burning smoke particles and

35 higher water vapor when approaching the monsoon season. The retrieved ω_0 and weighted-mean-radius of fine-mode aerosols from the SMART–s showed positive correlations with the H_2O (R = 0.81 for ω_0 at 330 nm and 0.56 for volume-weighted-mean-radius), whereas the real-part of the refractive-index of fine-mode aerosol (n_f) showed negative correlations (R = −0.61 at 330 nm), which suggest that aerosol aging processes including hygroscopic growth (e.g., humidification and cloud processing) can be a major factor affecting temporal trends of aerosol optical properties. Retrieved n_f and ω_0 were closer to

40 those of the water droplet (i.e., n_f of about 1.33 [unitless] and ω_0 of about 1.0 [unitless]) under lower amounts of NO_2 during the measurement period; considering that the NO_2 amounts in the smoke may indicate aging of the plume after emission due to its short lifetime, the tendency is also consistent with active hygroscopic processes of the aerosols over this area. Retrieved UV aerosol properties from the SMART–s generally support the assumed smoke aerosol models (i.e., spectral shape of aerosol absorption) used in current NASA's satellite algorithms, and their spectral ω_0 retrievals from ground and satellites showed

45 good agreements (R = 0.73–0.79). However, temporal and spectral variabilities of the aerosol absorption properties in the UV emphasize the importance of a realistic optical model of aerosols for further improvements in satellite retrievals.

1 Introduction

Significant spatiotemporal variabilities of the aerosols in the atmosphere complicate understanding of their scattering and absorption of the solar irradiance, which results in one of the largest uncertainties in predicting future climate (IPCC, 2013;

50 Gliß et al., 2021; Myhre et al., 2013 *and references therein*). The dominant fraction of the aerosols over the globe cools the atmosphere by reflecting solar irradiance, whereas some species (e.g., black carbon in the smoke plumes) heat the air by absorbing sunlight (i.e., direct radiative effects [DRE]: Chylek and Coakley, 1974; Haywood and Boucher, 2000; Yu et al., 2006). Primary factors of aerosols affecting the DRE are their loading and their absorption properties (e.g., Takemura et al., 2002 *and references therein*), which are often defined as aerosol optical thickness (τ_{aer}; total extinction by aerosols) and single-

55 scattering-albedo (ω_0; a ratio of the scattering to total extinction by aerosols), respectively. The ω_0 is calculated from complex refractive indices ($n+ik$; where n and k are a real and imaginary part, which depends on chemical composition) and particle size distribution (PSD), by assuming a spherical (Mie, 1908) or more sophisticated shape (e.g., Mishchenko et al., 2003; Yang et al., 2007). The ω_0 of non-absorbing aerosols (e.g., sea salt, sulfate, and nitrate particles) is close to 1.0 [unitless] with a relatively flat spectral shape, whereas it decreases down to about 0.7 [unitless] for absorbing aerosols (e.g., smoke and dust

60 particles) with significant spectral gradients (e.g., Dubovik et al., 2002; Eck et al., 2013; Müller et al., 2011; Sayer et al., 2014). Meteorological condition and aerosol hygroscopicity are also the key parameters affecting ω_0 since increased water content in the particles change the n, k, and PSD, which enhances light-scattering and results in higher ω_0 than dry particles (e.g., Jefferson et al., 2017; Li et al., 2019; Tao et al., 2014).

Decades of efforts have led to remote sensing techniques from both ground and satellite providing reliable τ_{aer}

65 retrievals over major parts of the globe (e.g., Giles et al., 2019; Hsu et al., 2019; Levy et al., 2013), whereas other aerosol properties retrieved from satellites are yet limited and relatively more uncertain due to the lower measurement sensitivity and

2

surface contributions (e.g., Jeong et al., 2016; Moosmüller et al., 2009). However, recent studies using more measurement parameters (e.g., multi-angle polarimetric measurements) showed promising results to provide reliable aerosol properties and constituents from satellites (e.g., Dubovik et al., 2019; Li et al., 2019). Globally networked ground-based instruments have

70 provided reliable optical and physical properties of aerosols (e.g., n, k, ω_0 and PSD), which are less affected by surface reflectance and acquire sufficient information content from multiple observation geometries (e.g., Dubovik and King, 2000; Jeong et al., 2020; Nakajima et al., 2020; Sinyuk et al., 2020). Satellite-based retrievals have utilized the aerosol properties from ground-based instruments as key constraints to expand upon their limitations (e.g., Hsu et al., 2019; Levy et al., 2013; Sayer et al., 2014).

75 Wildfires and prescribed fires have burned about 3.5% of Earth's ice-free land surface each year from 2001 to 2010 (Randerson et al., 2012) and emit a significant fraction of global aerosols and their precursors into the atmosphere. The biomass-burning aerosols (or smoke) consist primarily of carbonaceous aerosols (black and organic carbon), inorganic particles (e.g., potassium, chloride, sulfate, inorganic salts, and trace minerals), and inorganic and organic vapors (Hodshire et al., 2019 *and references therein*). Particularly primary and secondary organic aerosols, which account for a substantial fraction

80 of fine-mode smoke aerosols, comprise various compounds with enormously different volatility, oxidation, and hygroscopic properties (Xu et al., 2017 *and references therein*). Due to the reactivity and diversity of smoke particles, the ω_0 evolves with its environment (i.e., location and season), age, mixing state, and emission source of the plume (e.g., Eck et al., 2013; Haywood et al., 2003; Konovalov et al., 2017). In addition, Petters et al. (2009) reported that a major fraction of the smoke aerosols are already cloud-condensation-nuclei (CCN) active, and do not require chemical conversion to be more hygroscopic particles for

85 cloud formation and wet deposition, which adds another complication in understanding the Earth's climate.

Numerous studies have utilized ground-, airborne-, and satellite-based remote sensing techniques to monitor the properties and aging processes of the smoke particles. For example, Haywood et al. (2003) compared aerosol properties (e.g., PSD, τ_{aer}, and ω_0) from the collocated AERONET (AErosol RObotic NETwork; Holben et al., 1998) and airborne in-situ measurements at Windhoek, Namibia in September 2000, which showed excellent agreements. Eck et al. (2013) analyzed the

90 seasonal trend of aerosol properties retrieved from the AERONET and OMI (Ozone Monitoring Instrument) over southern Africa for a 15-year period and reported that the ω_0 increases significantly as the burning season progresses. Pistone et al. (2019) compared the spectral ω_0 of smoke aerosols from six independent airborne- and ground-based remote-sensing/in-situ instruments in September of 2016 out of Walvis Bay, Namibia, which showed acceptable agreements within the known uncertainties of each instrument (relative differences less than about 0.03 [unitless] in mid-visible and less than about 0.05

95 [unitless] in near-infrared, depends on the instruments). Over Southeast Asia, a series of field campaigns including BASE-ASIA (Biomass-burning Aerosols in SouthEast Asia: Smoke Impact Assessment) in 2006 and 7-SEAS (Seven SouthEast Asian Studies) from 2008 to present aimed to characterize aerosol-meteorological interactions over the region, mostly focusing on the smoke plumes. Physicochemical and optical properties of smoke aerosols were analysed by utilizing intensive ground- and satellite-based instruments during the campaigns (e.g., Lin et al., 2013; Pantina et al., 2016; Reid et al., 2013; Tsay et al.,

100 2013, 2016).

3

One of the important characteristics of the carbonaceous aerosols is their significant spectral variabilities of optical properties in the ultraviolet (UV) wavelengths, which are associated with photolysis processes in the atmosphere, thereby affecting tropospheric photochemistry, human health and agricultural productivity (e.g., George et al., 2015 *and references therein*). A majority of previous studies utilized direct/diffuse irradiance instruments (e.g., UV–MultiFilter Rotating Shadowband Radiometer [UV–MFRSR], Brewer spectroradiometer) to retrieve ω_0 in discrete channels in the UV. However, as these instruments measure only two observation parameters per channel, the algorithms adopted different sources of measurements/assumptions to complement the insufficient information (e.g., *see Table 1 in* Corr et al., 2009). For instance, in the absence of additional collocated instruments, they assumed fixed asymmetry parameter and surface albedo from previous studies or climatology (e.g., Bais et al., 2005; Petters et al., 2003; Wetzel et al., 2003). Collocated AERONET instruments have provided more realistic constraints of aerosol properties to the UV–MFRSR measurements (e.g., PSD and n from visible [VIS] wavelengths; Corr et al., 2009; Krotkov et al., 2005a) for retrieving ω_0 in the UV. Trace gas absorption (e.g., O_3 and NO_2) is another source of error for the ω_0 retrieval using these instruments. To take into account the gas absorptions, Goering et al. (2005) simultaneously retrieved total column O_3 in addition to the τ_{aer}, and ω_0, by using the spectral feature of irradiance. Later, Taylor et al. (2008) added a wavelength-independent asymmetry parameter to the state vector, where both algorithms are based on the optimal-estimation method (OEM; Rodgers, 2000). Krotkov et al. (2005a) used the aerosol phase function calculated from n at 440 nm and PSD from the AERONET, and total column O_3 from the Brewer spectroradiometer, to retrieve ω_0 in the UV channels. To account for the NO_2 absorption, which is a significant error source of ω_0 retrieval for low aerosol loading, they added retrieved NO_2 from the Brewer spectroradiometer for their algorithm (Cede et al., 2006; Krotkov et al., 2005b). A SKYNET (SKY radiometer NETwork) instruments are a similar type of Sun-sky spectroradiometer to the AERONET, which provides ω_0 at discrete channels in the UV (i.e., 340 and 380 nm). The SKYNET algorithm accounts for the O_3 absorption by using its retrieved total column from its 315 nm channel (Nakajima et al., 2007; 2020). Accuracies of the ω_0 retrievals from the SKYNET depend on errors in measurement and calibrations for Sun and sky-scans, surface albedo, cloud contamination, and the version of the processing software (i.e., Skyrad pack), which showed relative high biases compared to the AERONET (up to 0.07 [unitless] at longer wavelengths). Recently, Mok et al. (2018) combined the AERONET (for n, PSD, τ_{aer}) and Pandora (for total column O_3 and NO_2) products to the UV–MFRSR measurements to retrieve spectral ω_0 in the UV, which showed excellent agreements with SKYNET in the UV (i.e., 340 and 380 nm) but lower correlations in the longer wavelengths (i.e., 673 and 870 nm).

In addition, spectral n and k provide information not only on optical properties but also the chemical composition and physical status. The k demonstrates the attenuation of light by particles, which is the key parameter for determining ω_0, whereas the n describes the phase of light scattering by the particles. Numerous studies have focused on measuring/retrieving the n and k by utilizing various techniques to understand the effects of atmospheric particles on climate forcing and tropospheric photochemistry. Table 1 summarized reported values of the n from the previous and current studies. Kim et al. (2010) retrieved the n (at 670 nm) of secondary organic aerosols (SOA) generated by oxidizing α-pinene, β-pinene, and toluene with O_3, NO_x, and sunlight. The retrieved n varied between 1.38 and 1.61 [unitless], and they suggested that the n of SOA depends on aerosol

4

135 mass concentration, oxidation chemistry, temperature, and aerosol aging. Liu et al. (2013) measured the n and k of SOA for 220 to 1200 nm using a variable angle spectroscopic ellipsometer, and reported a rapid increase of the n and k in the UV. The n of the three selected SOA ranged from 1.53 to 1.58 [unitless] at 310 nm, 1.49−1.52 [unitless] at 550 nm, and 1.48−1.50 [unitless] at 1000 nm. Shepherd et al. (2018) estimated the spectral n of urban, remote, and wood smoke aerosols from 460 to 760 nm based on the optical trapping method, and reported high values of n of the wood smoke aerosols (~1.58 [unitless])

140 compared to the other types (1.47–1.52 [unitless]). They also well summarized and compared their values of the spectral n to other studies in their paper. Sumlin et al. (2018) retrieved the spectral n and k (at 375 nm, 405 nm, 532 nm, and 1047 nm) of brown carbon aerosols emitted from controlled fire using burning sources at various geographic origins. They reported that the n varies between 1.5 and 1.7 [unitless] without meaningful dependencies on wavelength, moisture content, source depth, or geographic origin, whereas the k increases from 0.003 to 0.014 [unitless] as wavelengths vary from 532 to 375 nm. Biagio

145 et al. (2019) estimated the n and k (at discrete channels in 370–950 nm) of 19 mineral dust aerosols from different sources based on Mie calculations combining optical and size measurements. They reported higher k (lower ω_0) of dust particles in the shorter wavelengths, which also depends on the iron content of dust, but the source and wavelength-independent values of n ranged from 1.48 to 1.55 [unitless]. More recently, Womack et al. (2021) retrieved the n and k of biomass-burning aerosols from 13 controlled fires over a 360–720 nm spectral range using a broadband cavity-enhanced spectrometer combined with

150 PSD measurements. Their algorithm incorporates Mie and Rayleigh–Debye–Gans scattering theories to account for both spherical and non-spherical particles, and retrieved n to be about 1.55 – 1.60 [unitless] and k to be significantly high (~0.25 [unitless]) in the UV.

   To be closely in line with and continue such efforts, we deployed a set of instruments including the SMART–s (Spectral Measurements for Atmospheric Radiative Transfer–spectroradiometer; Jeong et al., 2018, 2020) and AERONET

155 during the pre-monsoon yet active biomass-burning season at Fang, Thailand in 2019. Specifically, we aim to suggest the benefit of simultaneous retrievals of aerosols and trace gases covering UV, which may provide useful information on their physicochemical processes. In addition, aerosol properties in the UV are also important for various satellite algorithms for deriving higher-order aerosol parameters (e.g., absorption and vertical distribution), for which reliable measurements remain sparse. Benefits of employing SMART–s, a major instrument we utilized for this study, include:

160 • sufficient spectral resolution and coverage for measuring both aerosols and key trace gases (e.g., O_3, NO_2, and H_2O retrievals from direct-Sun measurements), in turn, the high-temporal measurements of gaseous absorption help improve the accuracy of ω_0 retrieval;

  • instantaneous measurements of the Sun/sky spectrum, permitting aerosol spectral properties retrieved from an identical set of volumes;

165 • reliable radiometric calibration from about 330 to 820 nm by utilizing a NIST-traceable (National Institute of Standards and Technology) uniform spectral radiance source (accuracy of about 1% in the VIS–NIR [near-infrared] and about 2% in the UV wavelengths at an approximate 95% confidence level) to enable accurate retrievals of aerosol column properties (e.g., τ_{aer}, n, k, ω_0); and

- stable performance, field-deployable for a long period – the recent expansion globally of Pandora network operation is based on its reliability at various field conditions, and SMART–s is nearly identical to the Pandora instrument except for the spectrometer (extended-range from about 280 to 820 nm, with about 1 nm spectral resolution).

As this study is the first attempt to retrieve aerosol properties from the SMART–s near the source region of active and extensive biomass-burning, we summarized the experimental design, instrument characteristics, the radiometric calibration in Section 2. In Section 3.1, we compared the retrieved aerosol property retrievals (e.g., n, k, ω_0) from the SMART–s with those from collocated AERONET for consistency check. Analyses of temporal variations in aerosols and total column trace gases (i.e., NO_2, H_2O, O_3) retrieved from the SMART–s were described in Section 3.2. We also demonstrated the relationship between aerosol properties and trace gas abundances in this section. Section 3.3 discussed possible applications of the retrieved aerosol parameters for satellite algorithms and preliminary validation/comparison results. Summary and conclusions are given in Section 4.

2 Measurements and calibrations

2.1 Experimental Setup

The ground-based spectroradiometer observations have offered optimum inversion products of the atmosphere for validating/comparing those from collocated space-borne sensors; these are less affected by the surface reflectance and can acquire more informative products from their higher resolution of temporal, spectral (including polarization), and angular measurements. In addition, strategically networked ground-based instruments (e.g., Distributed Regional Aerosol Gridded Observation Networks or DRAGON; Holben et al., 2018) can supplement their limited spatial representation. As a part of the ongoing 7-SEAS, intensive observations were conducted during the pre-monsoon season in April-May 2019 over northern Thailand, specifically the Chiang Mai, Fang, and Doi Angkhang areas. The international collaborators deployed an sUAS (small Unmanned Aerial System) in a rotary-/fixed-wing configuration for ~130 flights to measure boundary-layer profiles of thermodynamics and aerosol size/absorption. A mini-lidar, surface measurements of trace gases, and multiple chemistry samplers are also collocated with the three AERONET and one SMART-s instrument during the campaign. As the SMART-s is located in the middle of large source areas of biomass burning during the season, it can provide useful information on carbonaceous aerosols and key trace gases despite its limited spatial coverage.

Figure 1 shows an example of spatial distributions of τ_{aer} at 550 nm (Hsu et al., 2019) from the Deep Blue (DB) aerosol algorithm applied to VIIRS (Visible Infrared Imaging Radiometer Suite) aboard the SNPP (Suomi National Polar-orbiting Partnership) satellite and the corresponding true-color image over Southeast Asia on 30 March 2019, when significant amounts of biomass-burning aerosols prevailed (τ_{aer} at 550 nm higher than 3.0 [unitless]). The DB aerosol algorithm and its extended family have been applied to various spaceborne spectroradiometers such as AVHRR (Advanced Very High Resolution Radiometer), SeaWiFS (Sea-viewing Wide Field-of-view Sensor), MODIS (MODerate resolution Imaging Spectroradiometer), VIIRS (Hsu et al., 2019), and current advanced multispectral imagers aboard geostationary satellites,

6

enabling the construction of long-term aerosol climate data records (CDRs). As previously stated, satellite retrievals provide reliable τ_{aer} as indicated in Figure 1b; the collocated SMART–s measurement is also presented in the colored circle (τ_{aer} = 3.1 [unitless]) which shows an excellent agreement with the DB τ_{aer} retrievals nearby (mean τ_{aer} = 2.93 [unitless] within 10 km of SMART–s). In an attempt to derive more comprehensive aerosol properties from satellites, previous studies actively utilized

205 UV measurements which are sensitive to aerosol absorption and vertical profile as well as τ_{aer} (e.g., Torres et al., 2013; Lee et al., 2021). Accurate aerosol optical models play a central role in the endeavor. However, due to the lack of a reliable aerosol property database in the UV, they typically made simple assumptions on the spectral features of aerosols to extrapolate the properties from longer wavelengths or adopted laboratory measurements. One of the ultimate goals of this study is to contribute to satellite retrievals by providing realistic aerosol optical models over the study domain, particularly in the UV, which will be

210 discussed in Section 3.3.

The collocated SMART–s and AERONET instruments are deployed on the rooftop of Fang hospital in Fang District, as shown in Figures 1c and 1d, which is located in a basin of northern Thailand. The population of Fang city is slightly higher than 116,000 in 2010, with a low level of traffic throughout the year. One of the main roads of the city (Chotana Rd.) is nearby the building (~50 m). However, we presume the effects of local emissions from the road to the aerosol and NO_2 amounts are

215 not dominant given the low level of local traffic and that major fractions of the aerosols and trace gases (e.g., NO_2) during this season are emitted from the biomass-burning over this area (Jena et al., 2015; Itahashi et al., 2018; Khodmanee and Amnuaylojaroen, 2021). Figure 1d shows an image of the deployed SMART–s and the Chotana road shown behind. Direct-Sun measurements of the SMART–s started on 8 March 2019, and acquired additional solar-almucantar scans since 19 March after about 10 days of stabilization (e.g., for checking stability under the field condition and fine-tuning the alignment in

220 tracking). The measurements finished on 2 May 2019. The AERONET instrument is installed on the same rooftop, about 5 m away from the SMART–s. In 2019, surface air temperature at Fang during the pre-monsoon season reached up to about 42°C during the daytime, and relative humidity gradually increased from March (~30%) to early May (~50%).

2.2 Measurements

The SMART–s instrument is originally developed by the Pandora network group at NASA (National Aeronautics

225 and Space Administration) / GSFC (Goddard Space Flight Center) and the unit (#5) used in this study is registered as Pandora #48. Most of the components of SMART–s are similar or identical to the standard Pandora instrument except for the spectrometer. The SMART–s spectrometer is made by the same manufacturer (AvaSpec-ULS2048x64, Avantes, cf. https://www.avantes.com/ last access on 8 June 2022) as the standard version, but covers a wider spectral range (i.e., 280 – 820 nm) with a lower spectral resolution (~1.0 nm full-width-half-maximum [FWHM] with ~3.7× oversampling). As the

230 Pandonia Global Network (PGN; Herman et al., 2009, 2015; cf. https://www.pandonia-global-network.org) is utilizing another type of extended-range spectrometer for their dual-detector system, we refer to this modified Pandora as SMART–s in this study. The spectrometer utilizes a 2,048 × 64 back-thinned Hamamatsu CCD with a symmetric Czerny-Turner system, and its spectrum covers O_2, O_3, NO_2, SO_2, HCHO, and H_2O gas absorption bands (Herman et al., 2015; Jeong et al., 2018). The optical

head consists of two rotating filter wheels; one includes neutral density (ND) filters, and the other contains bandpass filters (e.g., U340 and BP300 to block out-of-band (OOB) stray light from the near-UV and VIS wavelengths), ground-fused silica diffuser (diffuser hereafter; for NO_2, H_2O, and τ_{aer} retrieval), and an opaque filter for dark current measurements. By combining a variable exposure time (4–4,000 ms) and ND filters, it can measure radiances with a dynamic range up to an order of 10^7 [unitless], which enables the direct-Sun and sky-scans using a single detector throughout the day. Note that the field of view (FOV) for direct-Sun observations using the diffuser of this unit is about 2.8°, which is broadened to evenly distribute light passing through the optical head. Sky observations do not use the diffuser to allow more photons to reach the detector, of which the FOV is about 1.5°. The optical head is mounted on a Sun/sky-scanner and is connected to the spectrometer through a fiber-optic cable of 400 μm in diameter. The spectrometer inside an insulated enclosure is thermoelectrically cooled to stabilize its temperature throughout the day. The controlled temperature depends on the ambient temperature where the instrument is deployed due to the capacity of the thermoelectric cooler, and the spectrometer temperature is monitored for each measurement.

The SMART–s algorithm aims to obtain optimal information on aerosols and trace gases with minimum assumptions, which incorporates a series of retrievals from fundamental quantities (i.e., column amounts) to higher-order geophysical parameters (e.g., aerosol physicochemical properties and vertical profiles). Jeong et al. (2018) developed an τ_{aer} algorithm of the SMART–s based on the spectral Langley method, then compared the retrievals to collocated AERONET measurements at the NASA / GSFC which showed excellent agreements at all overlapping wavelengths (i.e., 330 nm, 380 nm, 440 nm, 500 nm, and 675 nm). Comparisons of the τ_{aer} from the AERONET and SMART–s during this field deployment are shown in Appendix A (*cf.* Figure A1 and A2). The trace gas algorithm of the SMART–s is designed for a relatively lower spectral resolution (FWHM~1.0 nm) and broader spectral coverage (280–820 nm) compared to the standard Pandora. For retrieving optically thick trace gases such as O_3 and H_2O, we utilize the spectral Langley method (*see* Appendix B; Jeong et al., 2018), whereas we adopt the spectral-fitting algorithm of Pandora for other optically thin species including NO_2 (Herman et al., 2009). Retrieved total columns of τ_{aer}, O_3, and H_2O in this study are compared with those from the collocated AERONET (for τ_{aer} and H_2O) and satellite retrievals (O_3 from the OMI and τ_{aer} from the VIIRS) during the measurement period in Section 3.2 and Appendix A. Jeong et al. (2020) developed an OEM-based algorithm using solar-almucantar sky-radiances and total column retrievals (e.g., τ_{aer}, O_3, NO_2, and H_2O) for retrieving spectral n, k, ω_0 and PSD of aerosols; details of the aerosol-column-property algorithm are in the study, key characteristics are included here in Appendix C.

For more than two decades, the AERONET has been supported by NASA to operate a global network of automatic Sun/sky-scanning spectroradiometers for acquiring aerosol information (Holben et al., 1998). The instrument measures discrete channels (i.e., 340, 380, 440, 500, 675, 870, 940, 1,020, and 1,640 nm) of solar irradiance with a 1.2° FOV, which takes about 10 s to scan all spectral filter wheels. The FWHMs of the bandpass filters are 2 nm for 340 nm and 380 nm, 25 nm for 1640 nm, and 10 nm for all other channels, whereas that of the SMART–s is about 1.0 nm for all wavelengths. The estimated uncertainty of τ_{aer} from the AERONET reference instrument is 0.002 [unitless], and those from general network instruments are about 0.01 [unitless] in the VIS–NIR, and are higher (~0.02 [unitless]) in the UV channels (Eck et al., 1999; Giles et al.,

2019). Note that the uncertainty of τ_{aer} from the SMART–s is slightly higher than the AERONET (~0.02 [unitless] in the VIS–NIR, ~0.03 [unitless] in the UV) due to the wider FOV (Jeong et al., 2018), which is more susceptible to forward scattering, and temperature sensitivity of the detector (Kinne et al., 1997). The current AERONET product provides n, k, ω_0 at 440 nm, 675 nm, 870 nm, and 1020 nm. As the Version 3 algorithm utilizes a vector radiative transfer model (Korkin et al., 2017), it can add a 380 nm channel for the UV-absorbing aerosols (Sinyuk et al., 2020). The recent version of instruments added hybrid sky-scan measurements to allow additional retrievals at solar zenith angle (θ_S) below 50°. To consider gas absorption, the Version 3 algorithm adopts a monthly climatology (1978–2004) of O_3 from the Total Ozone Mapping Spectrometer (TOMS), that of NO_2 (2004–2013) from the OMI, and retrieved H_2O using the 940 nm channel measurements (Sinyuk et al., 2020). Further information on the AERONET products is summarized in Giles et al. (2019) and Sinyuk et al. (2020). We utilized the Version 3 and level 2.0 products to compare retrievals from the SMART–s.

2.3. A combinative radiometric calibration method for Sun/sky spectroradiometer

The standard calibration procedure of the SMART–s includes spectral characterization/registration, linearity and offset correction, radiometric calibration, temperature and flat field correction, and stray light correction (Herman et al., 2015; Jeong et al., 2018; Müller et al., 2020). The PGN also regularly reports updates and standard calibration/validation results on its webpage (https://www.pandonia-global-network.org; Herman et al., 2009, 2015). Utilization of the absolute sky-radiances requires precise radiometric calibrations, which we suggest as a novel and combinative method for Sun/sky spectroradiometers in this study. As this field campaign is the first attempt to deploy a radiometrically calibrated SMART–s using the method, we summarized detailed results of the calibration for the sky scans in this section.

For the initial step of the radiometric calibration, we utilized a uniform spectral radiance light source in the Radiometric Calibration Laboratory (RCL) at NASA / GSFC. The RCL is a class 10,000 cleanroom facility that maintains a number of NIST-traceable integrating sphere sources. The integrating sphere source used in this study is referred to as Grande. Grande is a Spectralon-lined, 101.6 cm diameter integrating-sphere source with a 25.4 cm diameter output aperture, which can generate nine levels of light output. More detailed information and annual calibration reports of Grande are available at https://cf.gsfc.nasa.gov/ or in Gatebe et al. (2007). Figure 2a is an image of the SMART–s mounted in front of the Grande sphere source, and Figure 2b shows Grande's nine levels of spectral output in radiance units. Panel-c presents reported total uncertainty of the Grande sphere's spectral radiance at an approximate 95% confidence level when calibrated using a NIST irradiance standard. Different colors in Figures 2b and 2c indicate the different levels of Grande intensity. Due to relatively low intensity in the UV compared to the VIS-NIR (Figure 2b) in both the NIST-calibrated irradiance standard and the Grande source itself, the calculated uncertainty of the Grande radiance calibration in the UV is higher, and brighter light output provides more accurate intensity as shown in Figure 2c. During the light source calibration, the sensor changed its filter (UV band-pass) to detect the lower intensity of the Grande in the UV which results in the relatively higher uncertainties near 350 nm (see Figure 2c). Note that the measurement error covariance matrix of the OEM also accounts for such spectral radiometric uncertainties (*see* Appendix C and Jeong et al., 2020). The SMART–s repeated measurements of Grande ten times for each

filter combination (bandpass filters and neutral density filters). The deployment procedure of the SMART–s (or Pandora) includes the organization of the fiber-optic cable and the connection of one end of the cable to the spectrometer (the other end of the cable is fixed to the optical head). This process can affect light transmittance through the cable. For checking the stability of the fiber-optic cable during deployment, we organized the cable differently (i.e., re-rolled the cable every time with different diameters or arbitral layout), then reconnected the ports to the spectrometer at each time of the Grande measurements. Contamination of the front window of the optical head (e.g., raindrops, dew, dust, and insects) is also one of the largest error sources of radiometric measurements. During field deployments, we frequently check the front window and clean it when it is necessary. However, as cleaning the front window also can alter its optical transmittance, we artificially contaminated the front window (by finger, dust, and water) and cleaned it in the same way as we do during field deployments at every time of the Grande observations. In addition, other sources of short- and long-term temporal drift (e.g., spectrometer, filter transmittance) are monitored by pre- and post-mission calibration and the Langley fitting during deployments. Figure 3a shows the results of ten repeat measurements of Grande at its 9-lamps illumination level. The agreement of these repeat measurements indicates good temporal stability in SMART-s responsivity and the Grande output. Figure 3b shows the spectral calibration coefficient calculated from dividing the Grande intensity (Figure 2b) by the average value of the measured voltage count (Figure 3a), while the spectral precision of the Grande calibration (i.e., one standard deviation of ten occurrences of the measurements) is presented in Figure 3c. These results indicate that the precision of the radiometric calibration from the instrument is better than 0.5% in the VIS–NIR channels, and increases at shorter wavelengths to about 0.7% at 330 nm (i.e., the lower limit of the spectral coverage in this study). Radiometric sensitivity of the spectrometer to its temperature (T_{spec}) is also tested by controlling the T_{spec}, which is less than 0.4% at the entire spectral range for an extreme T_{spec} variability (i.e., $\Delta T_{spec} \sim 3°C$, which is less than 2°C under typical field condition). In general, the uncertainty of the laboratory radiance calibration including the light source and instrument stability is estimated to be better than 2.0% in the VIS–NIR, and 3.0% in the UV at an approximate 95% confidence level.

As typical radiative transfer models (e.g., Spurr 2006; Stamnes et al., 1988) simulate normalized radiances (i.e., radiance divided by solar irradiance as a unit of inverse steradian), reference solar spectrum is also a key parameter of converting raw voltage counts to sky-radiances of the identical unit of forward model calculations. Satellite instruments can directly measure solar irradiance using the same detector with a similar optical path of the earth-reflectance measurements so that a major fraction of calibration uncertainties (e.g., slit function, radiometric coefficient) is canceled out. Although ground-based instruments also measure the solar light using an identical detector as for the sky radiances, they sample the solar irradiance after it passed through the atmosphere. For that reason, their algorithms utilize other sources of the solar spectrum or estimate it from the measurements. The version 3.0 AERONET inversion algorithm utilizes solar irradiance from NOAA's (National Oceanic and Atmospheric Administration) Climate Data Record (Coddington et al., 2016; Sinyuk et al., 2020), and the SKYNET derives a conversion factor of the sky-radiances from direct-Sun measurements based on the solid-view-angle estimation algorithm (Uchiyama et al., 2018a, b). For hyperspectral instruments such as the SMART–s, a combination of the high-resolution solar spectrum and calibrated slit function is a key factor for retrieving the spectral aerosol properties, which

is particularly important at wavelengths shorter than 500 nm where spectral variability of the solar irradiance is significant (e.g., see Figure 4a).

In the second step of the radiometric calibration, the SMART–s algorithm estimates the reference solar spectrum by combining direct-Sun measurements, laboratory calibrations, and ancillary solar irradiance data. Raw voltage counts of the sky-scan measurements without bandpass filters can be expressed as follows (e.g., Uchiyama et al., 2018b):

$$V(\lambda) = C(\lambda) \int_{\Omega_{FO}} f(\Omega) I(\lambda, \Omega) d\Omega, \tag{1}$$

where V is the voltage count of a sky-scan measurement, λ is the wavelength, C is the sensitivity of the detector to the radiance, Ω_{FO} is the solid angle of the instrument's field of view (FOV) without bandpass filters, f is the response function of the radiometer's FOV, and I is the sky-radiance. To avoid saturation, the direct-Sun measurements utilize the diffuser with a spectral transmittance of $T_d(\lambda)$ which is measured using the Grande. The measured voltage count of the solar scan can be described as follows:

$$V_S(\lambda) = C(\lambda) T_d(\lambda) \int_{\Omega_S} f(\Omega) I_D(\lambda, \Omega) d\Omega + C(\lambda) T_d(\lambda) \int_{\Omega_{FD}} f(\Omega) I(\lambda, \Omega) d\Omega, \tag{2}$$

where V_S is the voltage count of direct-Sun measurement, Ω_S and Ω_{FD} are the solid angle of the Sun and FOV of the SMART–s with the diffuser, respectively. The I_D is direct component of solar measurements. The first term on the right-hand-side of Eq. (2) describes the contribution of direct solar irradiance, and the second term shows the scattered radiance within the FOV. Here we assume that Ω_S and Ω_{FD} are not wavelength-dependent within the SMART–s spectral range. We select the Langley calibration dates when τ_{aer} at 500 nm is less than 0.05 to minimize aerosol impacts and screen cloud-contaminated measurements. In addition, the SMART–s algorithm corrects contribution of Rayleigh scattering of the direct-Sun measurements, which is larger in the shorter wavelength (Jeong et al., 2018). Based on this process and criteria, we assume that the second term of the right-hand-side of Eq. (2) is negligible. However, unscreened thin cirrus cloud may generate diffuse light within the FOV more effectively than the aerosols due to its stronger forward scattering (e.g., Kinne et al., 1997). For plane-parallel solar irradiance measurements ($f = 1$), the V_S can be approximated as:

$$V_S(\lambda) \sim C(\lambda) T_d(\lambda) \int_{\Omega_S} I_D(\lambda, \Omega) d\Omega = C(\lambda) T_d(\lambda) F_{BOA}(\lambda), \tag{3}$$

where F_{BOA} is solar irradiance at the bottom of the atmosphere which can be described as:

$$F_{BOA}(\lambda) = \int_{\Omega_S} I_D(\lambda, \Omega) d\Omega = F_V(\lambda) [\sum_i m_i(\lambda) \tau_i(\lambda)]. \tag{4}$$

In Eq. (4), F_V and τ denote respectively the extraterrestrial solar spectrum and optical thickness of atmospheric constituents, which are derived from the Langley calibration by using the V_S in Eq. (3). The m is the optical air mass of each atmospheric species (e.g., aerosols, clouds, and gases). Then, the last step is normalizing the F_V to a known solar irradiance data for minimizing the remaining systematic calibration error by the following equation:

$$F_{Comb}(\lambda) = \frac{\bar{F}_{Trad}}{\bar{F}_V} F_V(\lambda), \tag{5}$$

11

365 where the $\bar{F}_{\text{Trad}}$ is the spectral mean value of solar irradiance using the traditional method (i.e., a high-resolution reference solar spectrum convoluted by the instrument's slit function, F_{Trad}) and $\bar{F}_{\text{V}}$ is that of F_{V} at wavelengths between 490–510 nm. The F_{Comb} is the final solar irradiance for the SMART–s algorithm derived by combining the laboratory/Langley calibration, and reference spectrum (i.e., Coddington et al., 2021 in this study). This spectral window (490–510 nm) is near the middle of the detector, and solar intensity is high with relatively fewer spectral variabilities. In addition, this spectral range avoids strong

370 gas absorptions. By using the spectral shape of the F_{Comb}, we expect uncertainties generated from the calibrated slit function are minimized. Despite the Sun/sky measurements undergoing empirical OOB stray light correction (Jeong et al., 2018), the remaining fraction may still be nonnegligible in the shorter wavelengths of UV (particularly wavelengths shorter than about 330 nm; see Figure 7c of Jeong et al., 2018). However, as the F_{Comb} is supposed to be affected by OOB stray light with a comparable degree of the sky-scan measurements due to their similar spectral shape, it can partially cancel out the remaining

375 portion of stray light in the sky-radiances. Figure 4a compares the F_{Comb} to convoluted solar irradiance from Gueymard (2004), Chance and Kurucz (2010), and Coddington et al. (2021), which shows generally good consistency in the entire spectral range of SMART–s. Figure 4b shows an example of spectral radiances using the different solar spectrums in panel-a. The colored symbols in Figure 4b indicate the wavelength node of the aerosol retrieval, which is carefully selected to avoid a strong gas absorption bands and major calibration errors discussed above. Figure 4c depicts relative biases of the sky-radiances using the

380 F_{Comb} to those using Gueymard (2004), Chance and Kurucz (2010), and Coddington et al. (2021) at the wavelength nodes convoluted using the calibrated slit function. The biases are generally smaller than about 2% at wavelengths longer than 500 nm, and are higher in the shorter wavelength up to about 10% at 330 nm. The relatively high discrepancies between the F_{Comb} and the other solar irradiances in the UV are attributable to uncertainties in slit function, remaining OOB stray light, and the F_{V}. Note that uncertainties in the slit function affect F_{Trad} which may be significant in the UV. We estimate the accuracy of

385 F_{V}, which doesn't require spectral convolution, is better than 4% in the UV and 2% in the VIS-NIR based on the accuracy of the spectral τ_{aer} retrievals. Therefore, the total error of the sky radiance is estimated to be better than 5% in the UV and 3% in the VIS-NIR at an approximate 95% confidence level. The impacts of the different sources of the solar spectrum on aerosol retrievals are discussed in Section 3.

We applied the aerosol retrieval algorithm to the measurements (both direct Sun and solar-almucantar scan) with

390 sufficient amounts of photons within the target spectral range (i.e., from 330 to 800 nm) as huge amounts of aerosols over the area (e.g., Figure 1b) may result in the low level of voltage counts below the detection limit (e.g., in terms of linearity and noise). Cloud-contaminated direct-Sun spectrums were screened by using their rapid temporal variability and spectral features (i.e., lower Ångström exponent of clouds), which are described in Jeong et al., (2018). Those for the solar-almucantar measurements were removed by checking the horizontal symmetry of the scan (i.e., between clockwise and counter-clockwise

395 half-circle scans) followed by the AERONET strategy (Jeong et al., 2020).

3 Results

3.1 Comparison with the AERONET

Jeong et al. (2020) applied the SMART–s algorithm to a year-long AERONET Sun/sky measurements in 2016 at Kanpur, India to assess the consistency of methodology. Retrieved volume-size-distribution, V(r), from the SMART–s showed excellent agreements in the fine-mode but minor discrepancies in the coarse-mode due to the different assumptions and constraints between the two algorithms; the AERONET retrieves V(r) at 22 radius nodes over the optically effective range (i.e., from 0.05 μm to 15.0 μm) constrained by smoothness together with the k, whereas the SMART–s assumes a bi-modal, lognormal distribution of the number-size-distribution N(r) (Dubovik and King, 2000; Jeong et al., 2020). Spectral ω_0 showed excellent agreements for all wavelengths from 440 nm to 1020 nm, with R ranging from 0.87–0.95 and RMSE (Root-Mean-Squared Error) / MBE (Mean-Bias Error) less than 0.012 [unitless] during that year-long period. In this section, we performed additional comparisons of aerosol property retrievals from SMART–s to those from collocated AERONET by utilizing their own measurements.

Figure 5 depicts coincident V(r)s from the AERONET and SMART–s, where major fractions of the aerosols are fine-mode smoke particles, and less but nonnegligible portions are coarse particles (e.g., transported dust from Saharan and Thar desert, dry areas of the Indo-Gangetic plain). Retrieved V(r)s from both instruments show generally good agreement, which is consistent with the previous study (Jeong et al., 2020). Regarding that the SMART–s V(r) retrievals showed better agreements to the AERONET when it is applied to the same measurements (Jeong et al., 2020), another major fraction of the discrepancies in Figure 5 is likely attributable to the different types of measurements (e.g., spectral information and radiometric calibration). Note that the SMART–s measurement is not sensitive to aerosols with a radius greater than the optically effective range (~10 μm; *see Figure 10 in* Jeong et al., 2020), and the SMART–s V(r) over this range (see long tails of the blue dashed-line) is mostly generated by assuming the lognormal shape of coarse-mode. Further studies to derive optimal information on aerosol size are underway (e.g., additional parameters for size distribution and/or additional modes). According to theoretical error estimates of the OEM-based algorithm in Jeong et al. (2020), high-spectral resolution of the SMART–s is beneficial for the fine-mode whereas a broader spectral-range of the AERONET is advantageous for both modes under the same level of radiometric accuracy. More detailed comparisons and relevant discussions on the V(r) between the two algorithms are summarized in Jeong et al. (2020).

To better understand and assess the two PSD retrievals at each size-bin, precise evaluation through reliable in-situ measurements, such as aircraft profiles from DISCOVER-AQ (Deriving Information on Surface Conditions from Column and Vertically Resolved Observations Relevant to Air Quality), KORUS-AQ (KORea U.S.-Air Quality) and sUAS, are essential. However, to the best of our knowledge, very limited studies compared the AERONET V(r) to collocated in-situ profile measurements of the PSD. Chauvigné et al. (2016) compared the PSD from AERONET (at 410 m a.s.l. altitude) to in-situ measurements at a higher altitude site in central France (i.e., 1465 m a.s.l.) over a one-year period, which showed relative

underestimation of AERONET (~40%). However, the in-situ measurement site in Chauvigné et al. (2016) may not fully represent the total column values, which can be associated with the biases. Schafer et al. (2019) compared the AERONET V(r) to in-situ aircraft profiles (altitude from about 150 to 5000 m, and radius range from 0.03 to 0.5 μm) over Maryland, California, Texas, and Colorado in the United States. They showed that fine-mode PSD parameters derived from AERONET and in-situ aircraft measurements showed generally good agreement (average difference of radius of peak concentration about 0.011 μm, and that of V(r) width about 0.03 μm), whereas differences of the V(r)s depend on particle radius and location (*see Figure 5 of* Schafer et al., 2019). The SMARTLabs (Surface-based Mobile Atmospheric Research & Testbed Laboratories; https://smartlabs.gsfc.nasa.gov) is developing a sUAS-based aerosol profiling instrument for collocated measurements of spectral absorption and size distribution, which can provide valuable data for assessments of the PSD and ω_0 from SMART–s. More precise validation/comparison studies are currently underway.

Figure 6 compares the retrieved ω_0 from SMART–s and AERONET at overlapping wavelengths (i.e., 440 nm in left panels and 675 nm in right panels) during the measurement period. The ω_0 retrievals from SMART–s in the upper panels of Figure 6 (a and b) used the F_{Trad}, whereas those in lower panels (c and d) utilized the F_{Comb}. In general, all cases showed acceptable agreements with absolute mean-bias errors (MBE) and root-mean-square errors (RMSE) less than 0.02 [unitless], and R ranging from 0.77 to 0.82 [unitless]. The ω_0 of SMART–s was better correlated with that of AERONET in the shorter wavelength (i.e., 440 nm) due to the higher sensitivity of aerosols from the higher τ_{aer}. In addition, the F_{Comb} generated more consistent ω_0 retrievals of SMART–s with the AERONET than those using the F_{Trad}, with the slightly lower RMSE / MBE and higher R. Figure 7a presents mean values of the spectral τ_{aer} from SMART–s and AERONET during the measurement period, which showed excellent agreement over the SMART–s spectral coverage. Panel-b of Figure 7 shows those of the spectral ω_0 from the AERONET and SMART–s using different solar irradiances. While both versions of the ω_0 values from SMART–s exhibit strong absorption in the UV, the one using F_{Comb} showed smoother spectral variability, particularly in the UV, which is selected for the SMART–s retrievals hereafter. Slight relative low biases of the ω_0 from SMART–s compared to that from AERONET were also found when the SMART–s algorithm was applied to the same AERONET measurements at Kanpur, India, which are however still within the uncertainty range of the AERONET and SMART–s retrievals (Jeong et al., 2020). Note that the AERONET also provides τ_{aer} and ω_0 at longer wavelengths (e.g., 870 nm and 1020 nm), which are not presented in this figure.

In Figure 8a, the spectral n of fine- (n_f) and coarse-mode (n_c) retrieved from the SMART–s shows comparable values with the previous studies in Table 1 ranging from about 1.5 to 1.55 [unitless] with smooth spectral dependencies in the UV; higher values of n of the coarse-mode were found in the UV whereas those of the fine-mode were lower. These values were slightly higher than those from the collocated AERONET by about 0.01–0.04 [unitless]. Note that the AERONET retrieves a value n for all particle sizes, whereas the SMART–s retrieves each size mode (*see* Appendix C or Jeong et al., 2020), which may result in these differences under the assumption of lognormal size distribution. Regarding the fine-mode dominated smoke aerosols over the site (*cf.* Figure 5), n from the AERONET largely represents the contributions of the fine-mode, and differences between the n_f from SMART–s and n from AERONET are within known uncertainties of the AERONET (Sinyuk

14

et al., 2020) and SMART–s (Jeong et al., 2020). As reported in previous studies and spectral ω_0 retrievals in Figure 7b, the spectral k from SMART–s increased significantly in the shorter wavelengths, particularly in the fine-mode (*cf.* Figure 8b).
465 However, as the k retrievals of each mode have cross-correlated measurement sensitivity, separate analysis of each mode may have relatively larger uncertainties than the case of the n retrievals (*cf.* Appendix C and Figure A5). More detailed temporal and spectral analyses of aerosol optical properties from the SMART–s are given in the following sections and scatter plots of the n, k, and PSD between the two instruments are shown in Appendix D.

Validation or comparison of the UV aerosol properties from the SMART–s remains challenging due to the limited
470 coincident measurements. As discussed for Figure 5, in-situ profile measurements onboard the aircraft or sUAS platforms may provide reliable sets of data for validation. UV aerosol properties retrieved from other collocated instruments (e.g., Mok et al., 2018; Nakajima et al., 2020) can also offer useful data for checking consistency and redundancy. The spectral ω_0 retrievals from SMART–s are mainly determined by the ratio of the sky radiances to the τ_{aer}; highly absorbing aerosols result in the lower level of the sky radiances at a given τ_{aer}. Reliable spectral τ_{aer} from the SMART–s from 330 nm to 800 nm supports its
475 consistent radiometric performance (e.g., linearity, OOB stray light) over the wavelength range (Jeong et al., 2018). As the SMART–s measures sky radiances using the identical detector but without a diffuser, we expect comparable radiometric accuracy of the spectral sky measurements with relatively higher uncertainties in the UV as discussed in Section 2.3. Note that our best estimate of the accuracy of the spectral radiance is demonstrated in the measurement error covariance matrix, thereby considered in the estimated retrieval error (*see* Appendix C and Jeong et al., 2020).

480 **3.2 Temporal variations and relationship between aerosol properties and trace gases**

Total column amounts of trace gases and aerosols are basic and essential quantities not only for understanding their amounts and significance with variations over time but also for providing key constraints for higher-order retrievals (e.g., Jeong et al., 2018; 2020). Direct-Sun measurements of the SMART–s, AERONET, and Pandora provide very accurate retrievals of these parameters, which thereby have been used to validate/compare various satellite products over the globe.
485 This section presents general characteristics and temporal trends of the basic quantities retrieved from the SMART–s (i.e., τ_{aer}, total column amounts of O_3, NO_2, and H_2O), then analyzes higher-order retrievals of aerosol properties by comparing them with these quantities.

Figure 9 shows temporal variations of the τ_{aer} at 500 nm and total column amounts of NO_2, H_2O, and O_3 during the entire deployment period from the SMART–s and AERONET. The red circles in Figure 9a demonstrate aerosol optical
490 thickness at 550 nm from the VIIRS DB product, and those in Figure 9d depict OMI retrievals based on the TOMS (Total Mapping Spectrometer) Version 8.5 algorithm (Bhartia and Wellemeyer, 2002). In general, the τ_{aer}, H_2O, and O_3 retrievals from SMART–s showed excellent agreements with those from the AERONET, VIIRS, and OMI during the measurement period (see statistical values in Figures 9a, 9c, and 9d). Scatter plots of these parameters are shown in Appendix A (Figure A2).

15

495   Itahashi et al. (2018) analyzed high values of NO_2 from winter to pre-monsoon seasons over Southeast Asia based on satellite retrievals (i.e., SCanning Imaging Absorption spectroMeter for Atmospheric CHartographY, or SCIAMACHY; Bovensmann et al., 1999) and model calculations (i.e., Community Multi-scale Air Quality, or CMAQ), and reported that emissions from biomass-burning are attributable to the seasonal variation. They also estimated contributions of biomass-burning emissions to the total column NO_2 to be about 28% during 2003–2008 which was up to 58% in March 2004.

500   Khodmanee and Amnuaylojaroen (2021) estimated the contribution of biomass-burning to the NO_2 concentration over northern Thailand in March 2014 to be higher than 90% based on the WRF-Chem (Weather Research and Forecasting model with Chemistry) calculations. Another WRF-Chem study suggested that increase of NO_2 due to the biomass-burning emission is up to about 60% over Southeast Asia from March to May 2005 (Jena et al., 2015). During the measurement period, a large amount of NO_2 from the SMART–s is also accompanied by the high τ_{aer} at 500 nm with a correlation coefficient (R) of about 0.74,

505   which indicates the common emission sources (i.e., biomass-burning) of aerosols and NO_2 during the events as shown in Figure 9a and 9b.

        Interaction between atmospheric H_2O and aerosols is one of the primary factors in determining aerosol scattering and absorption properties (e.g., Burgos et al., 2019). Particularly for organic aerosols, molar mass and water content are dominant parameters for characterizing their phase state (e.g., Koop et al., 2011). The moisture-induced phase transition of organic

510   particles from a glassy to a semisolid state also accelerates the uptake of reactive gases in the atmosphere by decreasing viscosity and increasing diffusivity (Shiraiwa et al., 2011). In addition, the condensed water provides a medium for multiphase reactions, thus activating the gas-to-particle conversion of inorganic and organic molecules (Herrmann et al., 2015). The formation of the secondary species through the heterogeneous reactions generates further feedback to the aerosol-atmosphere system by enhancing water vapor absorption and hygroscopicity of aerosol particles (e.g., Tang et al., 2016; Wu et al., 2018).

515   Serving as cloud-condensation-nuclei (CCN), the physicochemical states of aerosols strongly influence cloud microstructure, thereby affecting the radiative properties of clouds, circulation and thermodynamics of the atmosphere (e.g., DeMott et al., 2010). During the intermediate period from dry to monsoon season in 2019, column precipitable H_2O gradually increases from about 1 cm in March to over 3 cm in May as shown in Figure 9c. Note that these mutually interacting species (i.e., τ_{aer}, NO_2, H_2O) are retrieved simultaneously from the same solar measurements using the ground-fused silica diffuser, which can provide

520   valuable information for further studies. Temporal variation of ozone in Figure 9d is mostly associated with fractions in the stratosphere, which also gradually increased from March (~250 DU) to May (~275 DU). Although the total column O_3 is not necessarily relevant to the major topic of this study, it is one of the key constraints of the future algorithm for estimating its tropospheric amounts (Jeong et al., 2020). It should also be noted that the SMART–s covers the O_3 Chappuis band in the VIS, which can complement its lower spectral resolution than the standard Pandora for profile retrieval (e.g., Natraj et al., 2011).

525   Figure 10 presents temporal variations of the ω_0 and H_2O in panel-a, those of the n_f and n_c in panels (b) and (c), respectively. The red circles and black squares show the retrievals at 330 nm and 550 nm, respectively, and their error bars indicate estimated retrieval error (ε_{ret}) based on the optimal-estimation-method (OEM; e.g., Jeong et al., 2016; 2020, *and also see* Appendix C). Note that the ε_{ret} is calculated for each retrieval, which is an important merit of the OEM for relevant studies.

As shown in Figure 10a, the ω_0 and H_2O gradually increased as biomass-burning activities decreased approaching the monsoon season (R = 0.65 between ω_0 and time, and 0.70 between H_2O and time). Interestingly, the correlation between the ω_0 and H_2O was even higher (R = 0.81 for ω_0 at 330 nm) than their temporal trends as shown in this figure. Eck et al. (2013) reported a similar increasing trend of the ω_0 from long-term AERONET and OMI measurements over Southern Africa. They suggested that a trend of decreasing black carbon content (e.g., due to more smouldering rather than flaming combustion) in the aerosol composition during the progress of burning can be a major reason than aerosol growth through aging, coagulation, or hygroscopic swelling, since size-related aerosol parameters such as Ångström exponent (AE) and volume-median-radius did not show a meaningful seasonal trend. However in this study, the retrieved n_f time series in Figure 10b exhibited a slightly decreasing trend over time with reliable retrieval accuracy ($\varepsilon_{ret} = 0.031 \pm 0.015$ [unitless]); this is consistent with the effects of the hygroscopic growth of aerosols, for which n_f values decrease (or get closer to the n of water) as a particle grows by water vapor uptake (e.g., Flores et al., 2012; Valenzuela et al., 2018). Meanwhile, the n_c retrievals are estimated to be highly uncertain ($\varepsilon_{ret} = 0.13 \pm 0.04$ [unitless]) due to the very limited information on coarse-mode aerosols as shown by large standard deviations in Figure 10c; the high values of ε_{ret} are attributable to the SMART–s spectral range, which is narrower than that of the AERONET, and fine-mode dominated smoke aerosols over this area (*cf.* Figure 5).

To further investigate the effects of H_2O on biomass-burning aerosol properties over the experiment regions, we have also examined the relationships of variations in n_f, ω_0, weighted-mean-radius of fine-mode and AE with changes in H_2O amounts. The upper panels of Figure 11 (panel-a and -b) compare the retrieved n_f and ω_0 to the total column amount of H_2O during the period. As previously discussed, the n_f is negatively correlated with the H_2O (R ranging from −0.57 to −0.61), whereas the ω_0 showed a high positive correlation for both the UV and longer wavelengths (R = 0.74 – 0.81). Lower panels of Figure 11 (panel-c and -d) show the relationship between the weighted-mean-radius of fine-mode and AE (*y*-axis) to column precipitable H_2O (*x*-axis) from the SMART–s. Figure 11c shows two types of weighted mean radius; area-weighted-mean-radius (r_a; or often called effective radius) and volume-weighted-mean-radius (r_v). The r_a has a proportional relationship with light extinction by particles, which is utilized by aerosol retrievals including the SMART–s algorithm, whereas the r_v has a linear relationship with volume-growth of aerosols. The r_a and r_v of fine-mode are calculated by the following equations, where the radius of 0.01 μm and 0.7μm are the lower and upper size-limit of the fine-mode particles, respectively:

$$r_a = \frac{\int_{0.01\mu m}^{0.7\mu m} r^3 N(r) dr}{\int_{0.01\mu m}^{0.7\mu m} r^2 N(r) dr} \tag{6}$$

$$r_v = \frac{\int_{0.01\mu m}^{0.7\mu m} r^4 N(r) dr}{\int_{0.01\mu m}^{0.7\mu m} r^3 N(r) dr} \tag{7}$$

As shown in Figure 11c, both the r_a and r_v showed a positive correlation with H_2O (R = 0.42 and 0.56, respectively), which is higher for the r_v. The short wavelength range AE is another good indicator of the fine-mode particle size (Reid et al., 1999; Eck et al., 2001), which is known to have a negative correlation with the size. The AE and absorbing AE (AAE) are calculated as follows:

$$AE = -\frac{\ln[\tau_{aer}(\lambda_1)/\tau_{aer}(\lambda_2)]}{\ln(\lambda_1/\lambda_2)}, \tag{8}$$

$$AAE = -\frac{\ln[\tau_{abs}(\lambda_1)/\tau_{abs}(\lambda_2)]}{\ln(\lambda_1/\lambda_2)}, \tag{9}$$

where τ_{abs} is the absorbing aerosol optical thickness (Equation 10):

$$\tau_{abs} = (1 - \omega_0)\tau_{aer}. \tag{10}$$

The AE calculated using both pairs of wavelengths showed a negative correlation with the H_2O (R ranging from -0.46 to -0.38).

NO$_2$ in the smoke plume may contain information on the degree of aging after emission; the lifetime of NO_2 is short (typically less than a few hours) and the brown carbon uptakes NO_2 by photochemical processes, thus NO_2 concentration likely decreases through the aging processes of the smoke plumes (e.g., Laskin et al., 2015). Therefore, lower values of the n_f (Figure 12a) and higher values of the ω_0 (Figure 12b) at lower amounts of NO_2 (likely related to the aged plume) support that their temporal variations may also be associated with accelerated aging processes of smoke aerosols by the increased H_2O. Even with the lower correlations, the size-related parameters in Figures 12c and 12d also indicate that smoke aerosols are likely growing under lower amounts of NO_2 during the pre-monsoon period; NO_2 showed a negative correlation with r_v and positive correlation with AE. However, note that the correlations of n_f, ω_0, r_v and AE with NO_2 also can be attributed to independent trends of emission and photochemical reactions of NO_2, which are not necessarily associated with the aerosol aging processes. More sophisticated studies combining model simulations and intensive measurements may be able to clarify relationships between NO_2 and aerosol properties. In general, the results in Figures 10–12 suggest that aerosol aging processes including hygroscopic growth also can be a critical parameter impacting temporal trends of aerosol optical properties over this area, in addition to previously suggested factors over South Africa (e.g., change of burning sources and conditions in Eck et al., 2013). Overall, such comparisons suggest the potential benefit of simultaneous measures of trace gases and aerosols for understanding atmospheric physicochemical processes.

3.3 UV-VIS-NIR aerosol absorption properties for satellite algorithms

The continuous UV-NIR aerosol property information retrieved from SMART-s can be useful not only for validating the satellite aerosol products, but also for fine-tuning appropriate aerosol models used in the satellite aerosol retrieval algorithm. The operational aerosol algorithm of OMI (OMAERUV; Torres et al., 2013) utilizes radiances at 354 nm and 388 nm for retrieving the τ_{aer} and ω_0. They assumed a ratio of k at 354 to that at 388 nm as 1.2 for smoke aerosols to account for the spectral absorption effects of organic carbon (Jethva and Torres, 2011; Jeong et al., 2016). They derived a monthly climatology of aerosol layer height (ALH) from observations by CALIOP (Cloud-Aerosol Lidar with Orthogonal Polarization) as ancillary data for the OMAERUV algorithm (Torres et al., 2013). Also, recently the improved ASHE (Aerosol Single-scattering albedo and Height Estimation; Lee et al., 2021) algorithm combines UV measurements from the OMPS-NM (Ozone Mapping and Profiler Suite Nadir Mapper) onboard the SNPP with the VIIRS radiances to provide retrieved ω_0 and ALH products as part of the VIIRS version 2 DB aerosol CDRs. For spectral dependences of the ω_0 in the UV, they assumed AAE

as 2.0 between 340 nm and 412 nm. Figure 13 shows an example of ω_0 retrievals at 340 nm (panel-a), 378 nm (panel-b) and 550 nm (panel-c) from the ASHE algorithm on the same day as Figure 1 (30 March 2019). Since the ASHE algorithm only performs retrievals when $\tau_{aer} > 0.5$ [unitless] and UVAI (UV Aerosol Index) > 0.7 [unitless], the spatial coverage of ω_0 in Figure 13 is reduced compared to that of τ_{aer} shown in Figure 1. The colored circles in this figure depict the collocated ω_0 retrievals from SMART–s. In general, the values of ω_0 retrieved from ASHE nearby the measurement site was comparable to that from the SMART–s, with its broader spatial coverage throughout the smoke aerosols of high τ_{aer} (*cf.* Figure 1b).

Temporal variations in ω_0 from the ASHE and SMART–s over the measurement site at overlapping wavelengths demonstrate their reasonable consistency, where both the retrievals indicate increasing trends during the measurement period with a higher temporal resolution of the SMART–s (*cf.* Figure 14a). The ASHE retrievals are available until 18 April 2019, since UVAI over the site decreased lower than the ASHE criteria likely due to the increased ω_0 over the period. Figure 14b compares the collocated ω_0 from ASHE and SMART–s during the measurement period, which showed good agreement between these two at ASHE's retrieval wavelengths. Higher correlations between the ASHE and SMART–s were found in the shorter wavelengths (R = 0.79 at 340 nm) due to the higher sensitivity of UV radiances to aerosol absorptions. The MBE and RMSE were lower than 0.02 [unitless] for all wavelengths. Note that the θ_S at Fang near the overpass time of VIIRS is small, whereas the SMART–s measures almucantar radiances θ_S from 40 to 75°. The average time difference between the ASHE overpass time and the closest SMART–s retrieval during the period was about 3 hours, and only samples with a time difference of fewer than 3 hours are shown in this figure. However, the difference of time between the ASHE and SMART–s still may affect the comparison in Figure 14, which can be improved by refinements of the scan strategy (e.g., hybrid scan of the AERONET version 3.0) for extending retrieval criteria of the θ_S.

AERONET sites in regions affected by biomass-burning smoke typically had AAE (440–870 nm) ranging from 1.0 to 2.0 [unitless] with values closer to 1.0 [unitless] indicating a greater contribution of black carbon and AAE near 2.0 [unitless] indicating increased organic-to-black carbon ratios (Giles et al., 2012). Figure 15a presents temporal variations in the AAE using different wavelength pairs calculated from the SMART–s τ_{aer} and ω_0. The AAEs calculated from UV wavelength and 550 nm pairs were comparable to the assumed value of the ASHE algorithm (2.04 ± 0.27 [unitless] for 340–550 nm pair, 1.94 ± 0.33 [unitless] for 378 nm and 550 nm pair) with non-negligible temporal variabilities ranging from about 1.3 to about 2.6 [unitless]. The AAE calculated using the 340–412 nm wavelengths pair, which is the actual pair for the ASHE inversion, showed much higher values (2.69 ± 0.35 [unitless]). Such discrepancies between the SMART–s retrievals and assumptions of aerosol properties in the ASHE algorithm may propagate to the differences in Figures 13 and 14. However, the retrieval errors are contextual, meaning that other error sources (such as uncertainties in the retrieved τ_{aer}, assumed size distribution in the aerosol optical models, etc.) can also contribute to the discrepancies, which makes it difficult to quantify the contribution of the AAE uncertainties to the retrieval errors. A longer-term data record in the UV is therefore highly desired. Figure 15b shows temporal variation in the ratio of k_f at 354 nm to 388 nm (1.17 ± 0.05), which is in good agreement with the assumed value of the OMAERUV algorithm (i.e., 1.2 for smoke aerosols), but with significant temporal variabilities. Both panels in Figure 15 suggest that current assumptions of the UV aerosol properties in OMAERUV and ASHE algorithms are generally good

19

approximations. However, temporal and spectral variabilities of the aerosol optical properties, which are presented throughout this section, also emphasize the importance of realistic aerosol models in the UV for further improvements of satellite algorithms. High spectral-resolution of the aerosol optical properties covering the UV can also benefit recently launched or upcoming hyperspectral satellite sensors targeting atmospheric composition (e.g., Chance et al., 2019; Ingmann et al., 2012; Kim et al., 2020). The National Institute of Environmental Research of South Korea recently started to deploy standard Pandoras and a few SMART–s units over Asia to validate GEMS (Geostationary Environment Monitoring Spectrometer; Kim et al., 2020) aerosol and trace gas products as well as to improve the satellite algorithms. Thus, deployments of networked SMART–s can contribute to comparing/validating spatiotemporal variations of aerosol ω_0, which is a key parameter for understanding their aging processes and interaction with other environmental conditions (e.g., terrain and meteorology; *cf.* Figure 13 for an example of the spatial variability). These ground-based measurements will provide important long-term records of UV aerosol properties at multiple strategic sites over Asia.

4 Summary and Conclusions

The SMART–s was deployed during the pre-monsoon season in northern Thailand to perform direct-Sun and sky-radiance measurements near biomass-burning sources. In this study, we summarized the detailed radiometric calibration procedures and results. To optimize solar irradiance for the radiometric conversion, we combined the Langley and NIST-traceable integrating sphere calibration data with the high-resolution reference spectrum from Coddington et al. (2021). We estimate the total uncertainties in the sky-radiance measurements are about 5% in the UV and better than 3% in the VIS–NIR wavelengths. The total column amount of the τ_{aer} and H_2O from SMART–s showed excellent agreements with those from collocated AERONET measurements (R = 1.0 and 0.98, respectively). Total column O_3 retrievals from the OMI showed good consistency with those from the SMART–s (R = 0.95, RMSE and MBE less than 3.6 DU). During the measurement period from mid-March to early-May in 2019, the τ_{aer} was mostly large (frequently exceeding 2.0 [unitless] at 500 nm) and strongly correlated with total column NO_2 (correlation coefficient, R = 0.74), likely due to the high emissions of biomass-burning smoke. The ω_0 from SMART–s and AERONET at overlapping wavelengths (i.e., 440 nm and 675 nm) showed acceptable agreements within uncertainties of these instruments (R = 0.79 – 0.81 with RMSE and MBE less than 0.015 [unitless]). The SMART–s retrievals showed good agreements of fine-mode V(r) with those from the AERONET, which is dominated by the smoke aerosols during the period. The spectral ω_0 of smoke aerosols showed an abrupt decrease in the UV consistent with the understanding of absorption by carbonaceous aerosols.

One of the major merits of the simultaneous retrieval of trace gases and aerosols from SMART–s is that it allows informative analysis of physicochemical interactions in the atmosphere. Our analyses comparing the trace gases (i.e., H_2O and NO_2) and aerosol properties (e.g., ω_0, n, r_a, and r_v) suggest that aerosol aging processes including hygroscopic growth can be a critical factor affecting temporal trends of aerosol optical properties during the pre-monsoon period over northern Thailand. Firstly, the ω_0 and column precipitable H_2O gradually increased together as it approached the monsoon season, and the correlation between ω_0 and H_2O was generally higher (R = 0.74 – 0.81) than their temporal trends (R = 0.65 for ω_0 and 0.70

for H2O). Secondly, the area/volume-weighted radius of fine-mode also showed a positive correlation with the H_2O ($R = 0.42$ and 0.56, respectively). The third result supporting the conclusion is that the n_f from SMART–s showed a negative correlation with the total column H_2O ($R = -0.61$ for 330 nm and -0.57 for 550 nm), which is supposed to decrease (or get close to the n of water about 1.33 [unitless]) as the particle uptake water vapor. However, in this study, measurements are performed at only one location during a limited period, while characteristics of smoke aerosols can vary significantly by region and time due to different fuel types, combustion efficiency, and aging processes. A longer period of measurements from multiple sites may help to clarify/understand such relationships.

The UV radiances are useful for satellite algorithms to retrieve higher-order aerosol parameters (e.g., single-scattering albedo and aerosol layer height), as these are sensitive to aerosol absorption and vertical profile. However, due to the lack of information contents and reliable aerosol model covering the UV, the algorithms typically assumed the spectral optical properties of aerosols or adopted from laboratory databases (e.g., Jethva and Torres, 2011; Lee et al., 2021). The retrieved UV aerosol properties from the SMART–s showed generally good agreements with the current assumptions of the ASHE and OMAERUV algorithms, thereby reasonable consistency of the ω_0 from between the SMART–s and ASHE retrievals ($R = 0.73 - 0.79$, MBE and RMSE less than 0.02 [unitless]). However, temporal and spectral variabilities of aerosol absorption properties (e.g., ω_0 and k) in the UV emphasize the importance of a realistic aerosol model for further improvements of satellite retrievals. Recently launched (e.g., GEMS) and upcoming hyperspectral sensors on the geostationary orbit (e.g., Tropospheric Emissions: Monitoring of Pollution; Chance et al., 2019, and Sentinel–4; Ingmann et al., 2012) aim to derive diurnal variations of trace gases and aerosols. The SMART–s can provide key parameters of trace gases and aerosols for constraining and validating satellite algorithms from its higher temporal resolution retrievals. Further improvements of algorithms and instruments for acquiring better information content and more reliable products (e.g., adding spectral polarization measurements, and refinement of scanning strategy such as adding a hybrid scan of the AERONET) are currently underway.

Appendix A. Scatter plots between the SMART–s direct Sun retrievals and AERONET/satellite observations.

Direct-Sun retrievals from the SMART–s are analyzed and compared with other sources of retrievals in Section 3. However, this section additionally shows scatter plots of τ_{aer}, total column H_2O and O_3 from the SMART–s with those from AERONET and satellite measurements during the campaign period for validation and checking consistency. As reported by Jeong et al. (2018), spectral τ_{aer} from the SMART–s showed excellent agreements with the AERONET at all overlapping wavelengths as shown in Figures A1 and A2-a, which is also in good agreement with the VIIRS DB product (Figure A2-b). The total precipitable water vapor (H_2O) and total column ozone from the SMART–s also showed excellent agreements with the AERONET and OMI as shown in Figures A2-c and A2-d.

21

Appendix B. SMART–s ozone and water vapor retrieval algorithm

690   The spectral Langley method (Jeong et al., 2018) retrieves spectral τ_{aer} by subtracting gas optical thickness (τ_{gas}) from the total optical thickness (τ_{tot}); the SMART–s observation is beneficial for this procedure as it measures spectral features of the τ_{gas}. The SMART–s retrieves optically thick trace gases (i.e., O_3 and H_2O) by using a similar method but with narrower fitting windows of the trace absorption bands (i.e., 315–335 nm for O_3 and 550–680 nm for H_2O). Examples of the fitting results for the O_3 and H_2O are shown in Figure A3 and A4, respectively, and intercomparison results with other data are in

695   Appendix A during the campaign. The fitting model for O_3 retrieval includes linear polynomials, O_3 and SO_2 cross-sections, and Raman spectrum, whereas that for the H_2O utilizes linear polynomials, H_2O, O_3, and O_2 cross-sections. More detailed design and calibration procedures for the spectral Langley method are demonstrated in Jeong et al. (2018) and measurements for long-term validation/comparison results are currently underway, which will be reported in the following paper (Jeong et al., 2022; *to be submitted*).

700   ## Appendix C. SMART–s aerosol inversion algorithm

Spectral bands for the aerosol property retrieval are carefully selected to avoid strong absorption by the gases and to efficiently obtain maximum information on aerosols. For example, we avoided major O_2-A, O_2-B, O_2-O_2, and H_2O bands where each corresponding F_{Comb} is highly uncertain (see Figures 4a and 4b). Nodes of relative azimuth angle (ϕ_r) for the solar-almucantar scan and those of wavelengths for the retrieval are summarized in Table A1 with other parameters. VLIDORT

705   (linearized pseudo-spherical vector Discrete Ordinate Radiative Transfer) code generates the full Stokes' parameters and analytic weighting function of atmospheric and surface variables including aerosol properties (Spurr, 2006; Spurr et al., 2012, Spurr and Christi, 2014). The state vector (**x**; a vector with elements of retrieval parameters and control variables to fit the measurements using a forward model) consists of fine and coarse mode n and k, five parameters of the PSD, two aerosol layer-height parameters, and spectral surface albedo. The algorithm assumes aerosol number-PSD as a bi-modal lognormal shape as

710   follows:

$$N(r) = \frac{F_{num}}{\sqrt{2\pi} \ln \sigma_f} \frac{1}{r_f} \exp\left[-\frac{1}{2}\left(\frac{\ln r - \ln r_f}{\ln \sigma_f}\right)^2\right] + \frac{(1-F_{num})}{\sqrt{2\pi} \ln \sigma_c} \frac{1}{r_c} \exp\left[-\frac{1}{2}\left(\frac{\ln r - \ln r_c}{\ln \sigma_c}\right)^2\right], \tag{A1}$$

where $N(r)$ is the number-size distribution, and the r_f and r_c are fine- and coarse-mode mean radius, and the σ_f and σ_c are geometric standard deviation of each mode. The F_{num} is number fraction of fine mode. However, the assumed bi-modal lognormal shape may not adequately represent the true fine- or coarse-mode distribution in some cases such as volcanic

715   eruptions, aerosol aging, and cloud processing (Eck et al., 2010; 2013; 2018). The aerosol extinction profile is assumed to be a Gaussian shape as follows:

$$ALH(z) = W \frac{e^{-h(z-z_p)}}{\left[1+e^{-h(z-z_p)}\right]^2}, \tag{A2}$$

where ALH(z) stands for the aerosol layer height (i.e., vertical profile of aerosol extinction), and the W is normalization factor. z_p is the peak height and h is the vertical dispersion parameter of the Gaussian profile shape. *A priori* information of the z_p and h is extracted from climatology of reanalysis data (e.g., Modern-Era Retrospective analysis for Research and Applications, Version 2; Gelaro et al., 2017), which is however not sensitive to the solar almucantar measurements. In this study, we assumed the surface reflectance (ρ) is Lambertian, of which *a priori* data are obtained from merged satellite measurements. More details of the parameters and design of the algorithm can be found at Jeong et al. (2020).

Averaging kernel (**A**) of the OEM is a useful matrix for understanding the information content of a set of measurements and inversion method, of which elements show the sensitivity of retrievals to the true state (e.g., Rodgers, 2000; Jeong et al., 2020). The **A** is defined as follows:

$$\mathbf{A} = \mathbf{GK} = \frac{\partial \hat{\mathbf{x}}}{\partial \mathbf{x}}, \tag{A3}$$

where **G** is the gain matrix for representing the sensitivity of retrievals to the measurements and **K** is the weighting function matrix of which the elements are partial derivatives of each measurement with respect to the state vector. In the Equation (A3), each element of the **A** characterizes how the retrieval ($\hat{\mathbf{x}}$) responses to the true state (**x**). Diagonal elements of **A** ($D_\mathbf{A}$) indicate the sensitivity of each retrieval parameter using a set of measurements and an inversion method, whereas off-diagonal elements of an ith row ($R_\mathbf{A}$) demonstrate retrieval errors of $\mathbf{x}_i$ by cross-correlation with other parameters or by insufficient information contained in the measurements. Therefore, for an ideal inversion with an observing system, its **A** is close to an identity matrix (Rodgers, 1990). More discussion of **A** for the SMART–s is summarized in Jeong et al. (2020). Figure A5 shows an example of **A** from the SMART–s retrieval at Fang on 10 April 2019, when fine- and coarse-mode volume fractions were comparable and ω_0 was about 0.87 [unitless] with τ_{aer} about 1.06 [unitless] at 440 nm. Figure A5a presents the whole **A**, and the panel-b zooms to the PSD (indices from 1 to 5) and ALH parameters (indices of 6 and 7) as indicated as a green square in panel-a. The $D_\mathbf{A}$ of PSD parameters (diagonal elements of 1–5; order of r_f, σ_f, r_c, σ_c, and F_{num}) are close to one, which shows their sufficient retrieval sensitivity from the measurement. Particularly, $R_\mathbf{A}$ of the r_f and the F_{num} (see off-diagonal elements of the 1$^{\text{st}}$ and 5$^{\text{th}}$ rows in Figure A5b) have small absolute values, whereas those of σ_f, r_c and σ_c (rows from 2 to 4) are relatively high. As solar-almucantar measurements are not sensitive to the vertical profile of aerosols, $D_\mathbf{A}$ of the ALH parameters (z_p and h of indices 6 and 7) are low with their relatively higher values of the $R_\mathbf{A}$ for k_f and k_c. $D_\mathbf{A}$ of the n_f and n_c show their sufficient retrieval sensitivity at all wavelengths. In addition, the $R_\mathbf{A}$ of n_f for n_c and that of n_c for n_f were negligible which suggests that their retrieval sensitivity for each mode is independent and can be retrieved separately. However, the $R_\mathbf{A}$s of n_f and n_c demonstrate that they are also affected by the k_f and k_c. On the contrary, $R_\mathbf{A}$ of the k_f and k_c are low at most of the other parameters (i.e., n, PSD, ALH, and ρ), whereas the $R_\mathbf{A}$ of k_f at state vector k_c (or *vice versa*) shows high values of diagonal elements indicating retrieval sensitivity across the fine- and coarse-mode; therefore, we analyzed the ω_0 for both modes in this study. As well-recognized, retrieval sensitivity of the ρ is negligible which results in low values of the whole rows of ρ in Figure A5. We also limit the retrieval range of solar zenith angle (θ_S) up to 75° to minimize the effects of surface reflectance at high θ_S and viewing zenith angle (θ_V). Note that the **A** varies significantly depending on cases, and retrieval errors due to the interferences between

different parameters and/or lack of information content are considered by the error estimation method of the OEM (Rodgers, 2000; Jeong et al., 2020).

One of the important merits of the OEM is its theoretical formulations of retrieval errors, which are classified into four categories (Rodgers, 1990; 2000; Jeong et al., 2016; 2020): the smoothing error (ε_s), retrieval noise (ε_m), forward model error (ε_r), and model parameter error (ε_f). As the **x** contains the most dominant parameters of aerosols and quantifying uncertainties in the radiative transfer model is challenging, we neglect the (ε_r) and (ε_f). We defined retrieval error (ε_{ret}) as the square root of the sum of squared ε_s and ε_m, which represents the minimum uncertainty of the SMART-s aerosol inversions. Detailed descriptions and discussions of the ε_{ret} are summarized by Jeong et al. (2020).

Appendix D. Comparison of aerosol optical properties from the SMART–s and AERONET

Coincident retrievals of the ω_0, n, k, and V(r) are compared and discussed in Figures 5 to 10. The remaining scatter plots of these inversion parameters of the SMART–s and AERONET are shown in this section. Figure A6 compares aerosol inversion products from the SMART–s and AERONET (Version 3, Level 2.0). The upper panels compare the real part of the refractive index at (a) 440 nm and (b) 675 nm, and the middle panels are for the imaginary part. The lower panels compare (e) area- and (f) volume-weighted-mean-radii. Larger discrepancies between the SMART–s and AERONET were found for the n due to the lack of information content and different assumptions of the algorithms, whereas higher consistency appeared for the k as discussed for the ω_0. High agreements of the r_s and r_v were found between the two instruments as shown in Figures A6e and A6f (R = 0.86 with MBE and RMSE less than 0.016 μm).

Acknowledgments

Code/Data availability

The SMART–s data are also described at https://earth.gsfc.nasa.gov/climate/instruments/smartlabs, and available
from the contact email addresses on the webpage. The AERONET data are available at the https://aeronet.gsfc.nasa.gov
website.

Author contribution

The first and corresponding author (Ukkyo Jeong) led overall algorithm development, instrument calibration and
manuscript writing. Si-Chee Tsay supervised the overall activities for this study and is also in charge of the campaign for this
study. Nai-Yung Hsu and Jaehwa Lee provided the satellite retrievals for comparing the aerosol optical properties analyzed in
this study. David Giles and Brent Holben provided critical revision for aerosol retrievals as well as the overall manuscript.
John Cooper and James Butler provided the NIST-traceable light source for radiometric calibration, and also reviewed
instrument calibrations. Robert Swap was in charge of the Pandora network operation for the campaign and also supported
instrument maintenance. Sheng-Hsiang Wang and Comporn Chantara supported the local operation of the instruments
throughout the campaign periods and also reviewed the final manuscript. Hyungkee Hong, Donghee Kim and Jhoon Kim are
in charge of the Asian Network of the Pandora and the Geostationary Environment Monitoring Spectrometer, which provided
critical insight for this study. They also provided critical revisions for the manuscript.

Competing interests

The authors do not have any competing interests.

References

Bais, A. F.,Kazantzidis, A., Kazadzis, S., Balis, D. S, Zerefos, C. S., and Meleti, C.: Deriving an effective aerosol single
scattering albedo from spectral surface UV voltage measurements, Atmos. Environ., 39, 1093–1102,
https://doi.org/10.1016/j.atmosenv.2004.09.080, 2005.

Bhartia, P. K., and Wellemeyer, C. W.: OMI TOMS-V8 Total O_3 algorithm, in OMI Algorithm Theoretical Basis Document,
Vol. 2, NASA Goddard Space Flight Cent., Greenbelt, Md., USA, 15–32, 2002.

Biagio, C. D., Formenti, P., Balkanski, Y., Caponi, L., Cazaunau, M., Pangui, E., Journet, E., Nowak, S., Andreae, M. O.,
Kandler, K., Saeed, T., Piketh, S., Seibert, D., Williams, E., and Doussin, J.-F.: Complex refractive indices and single-

805 scattering albedo of global dust aerosols in the shortwave spectrum and relationship to size and iron content, Atmos. Chem. Phys., 19, 15503–15531, https://doi.org/10.5194/acp-19-15503-2019, 2019.

Bovensmann, H., Burrows, J. P., Buchwitz, M., Frerick, J., Noël, S., Rozanov, V. V., Chance, K. V., Goede, A. P. H.: SCIAMACHY: mission objectives and measurement modes, J. Atmos. Sci., 56, 127-150, 1999.

810

Burgos, M.A., Andrews, E., Titos, G., Alados-Arboledas, L., Baltensperger, U., Day, D., Jefferson, A., Kalivitis, N., Mihalopoulos, N., Sherman, J., Sun, J., Weingartner, E., and Zieger, P.: A global view on the effect of water uptake on aerosol particle light scattering. Sci. Data, 6, 157, https://doi.org/10.1038/s41597-019-0158-7, 2019.

815 Cede, A., Herman, J. R., Richter, A., Krotkov, N., and Burrows, J.: Measurements of nitrogen dioxide total column amounts using a Brewer double spectrophotometer in direct Sun mode, J. Geophys. Res., 111, D05304, https://doi.org/10.1029/2005JD006585, 2006

Chance, K., and Kurucz, R. L.: An improved high-resolution solar reference spectrum for Earth 's atmosphere measurements
820 in the ultraviolet, visible, and near infrared, J. Quant. Spectrosc. Ra., 111(9), 1289–1295. https://doi.org/10.1016/j.jqsrt.2010.01.036, 2010.

Chance, K., X. Liu, C. Chan Miller, G. Gonz lez Abad, G. Huang, C. Nowlan, et al.: TEMPO green paper: Chemistry, physics, and meteorology experiments with the tropospheric emissions: Monitoring of pollution instrument, Proc. SPIE 11151, sensors,
825 systems, and next-generation satellites XXIII, 111510B, https://doi.org/10.1117/12.2534883, 2019.

Chauvigné, A., Sellegri, K., Hervo, M., Montoux, N., Freville, P., and Goloub, P: Comparison of the aerosol optical properties and size distribution retrieved by sun photometer with in situ measurements at midlatitude, Atmos. Meas. Tech., 9, 4569–4585, https://doi.org/10.5194/amt-9-4569-2016, 2016.

830

Chylek, P. and Coakley, J.: Aerosols and Climate, Science, 183, 75–77, https://doi.org/10.1126/science.183.4120.75, 1974.

Coddington, O., Lean, J. L., Pilewski, P., Snow, M., and Lindholm, D.: A solar irradiance climate data record, Bull. Amer. Meteor. Soc., 97, 1265–1282, https://doi.org/10.1175/BAMS-D-14-00265.1, 2016.

835

Coddington, O., Richard, E. C., Harber, D. H., Pilewskie, P., Woods, T. N., Chance, K., Liu, X., and Sun, K.: The TSIS-1 hybrid solar reference spectrum, Geophys. Res. Lett., 48, e2020GL091709. https://doi.org/10.1029/2020GL091709, 2021.

Community Multiscale Air Quality Modeling System (CMAQ), USEPA, available at: https://www.epa.gov/cmaq/how-cite-cmaq, (accessed on 14 May 2021).

Corr, C. A., Krotkov, N, Madronich, S., Slusser, J. R., Holben, B. N., Gao, W., Flynn, J., Lefer, B., and Kreidenweis, S. M.: Retrieval of aerosol single scattering albedo at ultraviolet wavelengths at the T1 site during MILAGRO, Atmos. Chem. Phys., 9, 5813–5827, https://doi.org/10.5194/acp-9-5813-2009, 2009.

DeMott, P. J., Prenni, A. J., Liu, X., Kreidenweis, S. M., Petters, M. D., Twohy, C. H., Richardson, M. S., Eidhammer, T., and Rogers, D. C.: Predicting global atmospheric ice nuclei distributions and their impacts on climate, Proc. Natl. Acad. Sci., 107, 25, 11217–11222, https://doi.org/10.1073/pnas.0910818107, 2010.

Dubovik, O. and King, M.: A flexible inversion algorithm for retrieval of aerosol optical properties from Sun and sky radiance measurements, J. Geophys. Res.-Atmos., 105, 20673–20696, https://doi.org/10.1029/2000JD900282, 2000.

Dubovik, O., Holben, B., Eck, T., Smirnov, A., Kaufman, Y., King, M., Tanre, D., and Slutsker, I.: Variability of absorption and optical properties of key aerosol types observed in worldwide locations, J. Atmos. Sci., 59, 590–608, https://doi.org/10.1175/1520-0469(2002)059<0590:VOAAOP>2.0.CO;2, 2002.

Dubovik, O., Li, Z., Mishchenko, M. I., Tanré, D., Karol, Y., Bojkov, B., Cairns, B., Diner, D. J., Espinosa, W. R., Goloub, P., Gu, X., Hasekamp, O., Hong, J., Hou, W., Knobelspiesse, K. D., Landgraf, J., Li, L., Litvinov, P., Liu, Y., Lopatin, A., Marbach, T., Maring, H., Martins, V., Meijer, Y., Milinevsky, G., Mukai, S., Parol, F., Qiao, Y., Remer, L., Rietjens, J., Sano, I., Stammes, P., Stamnes, S., Sun, X., Tabary, P., Travis, L. D., Waquet, F., Xu, F., Yan, C., and Yin, D.: Polarimetric remote sensing of atmospheric aerosols: Instruments, methodologies, results, and perspectives, J. Quant. Spectrosc. Ra., 224, 474–511, https://doi.org/10.1016/j.jqsrt.2018.11.024, 2019.

Eck, T. F., Holben, B. N., Reid, J. S., Dubovik, O., Smirnov, A., O'Neill, N. T., Slutsker, I., and Kinne, S.: Wavelength dependence of the optical depth of biomass burning, urban, and desert dust aerosols, Journal of Geophysical Research, 104(D24), 31,333–331,349, https://doi.org/10.1029/1999JD900923, 1999.

Eck, T. F., Holben, B. N., Ward, D. E., Dubovik, O., Reid, J. S., Smirnov, A., Mukelabai, M. M., Hsu, N. C., O'Neill, N. T., and Slutsker, I.: Characterization of the optical properties of biomass burning aerosols in Zambia during the 1997 ZIBBEE field campaign, J. Geophys. Res., 106, 3425–3448, https://doi.org/10.1029/2000JD900555, 2001.

Eck, T. F., Holben, B. N., Sinyuk, A., Pinker, R. T., Goloub, P., Chen, H., Chatenet, B., Li, Z., Singh, R. P., Tripathi, S. N., Reid, J. S., Giles, D. M., Dubovik, O., O'Neill, N. T., Smirnov, A., Wang, P., and Xia, X.: Climatological aspects of the optical properties of fine/coarse mode aerosol mixtures, J. Geophys. Res., 115, D19205, https://doi.org/10.1029/2010JD014002, 2010.

875

Eck, T. F., Holben, B. N., Reid, J. S., Mukelabai, M. M., Piketh, S. J., Torres, O., Jethva, H. T., Hyer, E. J., Ward, D. E., Dubovik, O., Sinyuk, A., Schafer, J. S., Giles, D. M., Sorokin, M., Smirnov, A., and Slutsker, I.: A seasonal trend of single scattering albedo in southern African biomass-burning particles: Implications for satellite products and estimates of emissions for the world's largest biomass-burning source, J. Geophys. Res.-Atmos., 118, 6414–6432, https://doi.org/10.1002/jgrd.50500,

880   2013.

Eck, T. F., Holben, B. N., Reid, J. S., Xian, P. Giles, D. M., Sinyuk, A., Smirnov, A., Schafer, J. S., Slutsker, I., Kim, J. et al.: Observations of the interaction and transport of fine mode aerosols with cloud and/or fog in northeast Asia from AErosol RObotic NETwork and satellite remote sensing, J. Geophys. Res., 123, 5560–5587, https://doi.org/10.1029/2018JD028313,

885   2018.

Flores, J. M., Bar-Or, R. Z., Bluvshtein, N., Abo-Riziq, A., Kostinski, A., Borrmann, S., Koren, I., Koren, I., and Rudich, Y.: Absorbing aerosols at high relative humidity: linking hygroscopic growth to optical properties, Atmos. Chem. Phys., 12, 5511–5521, https://doi.org/10.5194/acp-12-5511-2012, 2012.

890

Gatebe, C. K., J. J. Butler, J. W. Cooper, M. Kowalewski, and M. D. King: Characterization of errors in the use of integrating-sphere systems in the calibration of scanning radiometers, Appl. Opt., 46, 31, 7640–7651, https://doi.org/10.1364/AO.46.007640, 2007.

895   Gelaro, R., W. McCarty, M. J. Suárez, R. Todling, A. Molod, Takacs, L., Randles, C. A., Darmenov, A., Bosilovich, M. G., Reichle, R., Wargan, K., Coy, L., Cullather, R., Draper, C., Akella, S., Buchard, V., Conaty, A., da Silva, A. M., Gu, W., Kim, G.-K., Koster, R., Lucchesi, R., Merkova, D., Nielsen, J. E., Partyka, G., Pawson, S., Putman, W., Rienecker, M., Schubert, S. D., Sienkiewicz, M., and Zhao, B.: The Modern-Era Retrospective Analysis for Research and Applications, Version 2 (MERRA-2), Bull. Amer. Meteor. Soc., 30, 5419-5454, https://doi.org/10.1175/JCLI-D-16-0758.1, 2017.

900

George, C., Ammann, M., D'Anna, B., Donaldson, D. J., and Nizkorodov, S. A.: Heterogeneous photochemistry in the atmosphere, Chem. Rev., 115, 4218−4258, https://doi.org/10.1021/cr500648z, 2015.

Goering, C. D., L'Ecuyer, T. S., Stephens, G. L., Slusser, J. R., Scott, G., Davis, J., Barnard, J. C., and Madronich, S.: Simultaneous retrievals of column ozone and aerosol optical properties from direct and diffuse solar voltage measurements, J. Geophys, Res., 110, D05204, https://doi.org/10.1029/2004JD005330, 2005.

Giles, D. M., Holben, B. N., Eck, T. F., Sinyuk, A., Smirnov, A., Slutsker, I., Dickerson, R. R., Thompson, A. M., and Schafer, J. S.: An analysis of AERONET aerosol absorption properties and classifications representative of aerosol source regions, J. Geophys. Res., 117, D17203, https://doi.org/10.1029/2012JD018127, 2012.

Giles, D. M., Sinyuk, A., Sorokin, M. G., Schafer, J. S., Smirnov, A., Slutsker, I., Eck, T. F., Holben, B. N., Lewis, J. R., Campbell, J. R., Welton, E. J., Korkin, S. V., Lyapustin, A. I.: Advancements in the Aerosol Robotic Network (AERONET) Version 3 database – automated near-real-time quality control algorithm with improved cloud screening for Sun photometer aerosol optical depth (AOD) measurements, Atmos. Meas. Tech., 12, 169–209, https://doi.org/10.5194/amt-12-169-2019, 2019.

Gliß, J., Mortier, A., Schulz, M., Andrews, E., Balkanski, Y., Bauer, S. E., Benedictow, A. M. K., Bian, H., Checa-Garcia, R., Chin, M., Ginoux, P., Griesfeller, J. J., Heckel, A., Kipling, Z., Kirkevåg, A., Kokkola1, H., Laj, P., Le Sager, P., Lund, M. T., Myhre, C. L., Matsui, H., Myhre, G., Neubauer, D., van Noije, T., North, P., Olivié1, D. J. L., Rémy, S., Sogacheva, L., Takemura, T., Tsigaridis, K., and Tsyro1, S. G.: AeroCom phase III multi-model evaluation of the aerosol life cycle and optical properties using ground- and space-based remote sensing as well as surface in situ observations, Atmos. Chem. Phys., 21, 87–128, https://doi.org/10.5194/acp-21-87-2021, 2021.

Gueymard, C. A.: The sun's total and spectral irradiance for solar energy applications and solar radiation models, Sol. Energy, 76, 4, 423–453, https://doi.org/10.1016/j.solener.2003.08.039, 2004.

Haywood, J., and Boucher, O.: Estimates of the direct and indirect radiative forcing due to tropospheric aerosols: a review, Rev. Geophys., 38, 4, 513-543, https://doi.org/10.1029/1999RG000078, 2000.

Haywood, J., Francis, P., Dubovik, O., Glew, M., and Holben, B.: Comparison of aerosol size distributions, radiative properties, and optical depths determined by aircraft observations and Sun photometers during SAFARI 2000, J. Geophys. Res.-Atmos., 108, 8471, https://doi.org/10.1029/2002JD002250, 2003.

Herrmann, H., Schaefer, T., Tilgner, A., Styler, S. A., Weller, C., Teich, M., and Otto, T.: Tropospheric aqueous-phase chemistry: Kinetics, mechanisms, and its coupling to a changing gas phase, Chem. Rev., 115, 10, 4259–4334, https://doi.org/10.1021/cr500447k, 2015.

Herman, J. R., Cede, A., Spinei, E., Mount, G., Tzortziou, M., and Abuhassan, N.: NO_2 column amounts from ground-based Pandora and MFDOAS spectrometers using the direct-Sun DOAS technique: Intercomparisons and application to OMI validation. J. Geophys. Res., 114, D13307. https://doi.org/10.1029/2009JD011848, 2009.

Herman, J. R., Evans, A., Cede, N., Abuhassan, I. P., and McConville, G.: Comparison of ozone retrievals from the Pandora spectrometer system and Dobson spectrometer in Boulder, Colorado. Atmos. Meas. Tech., 8(8), 3407–3418. https://doi.org/10.5194/amt-8-3407-2015, 2015.

Hodshire, A. L., Akherati, A., Alvarado, M. J., Brown-Steiner, B., Jathar, S. H., Jimenez, J. L., Kreidenweis, S. M., Lonsdale, C. R., Onasch, T. B., Ortega, A. M., and Pierce, J. R.: Aging Effects on Biomass Burning Aerosol Mass and Composition: A Critical Review of Field and Laboratory Studies, Environ. Sci. Technol., 53, 10007–10022, https://doi.org/10.1021/acs.est.9b02588, 2019.

Holben, B. N., Eck, T. F., Slutsker, I., Tanré, D., Buis, J. P., Setzer, A., Vermote, E., Reagan, J. A., Kaufman, Y. J., Nakajima, T., Lavenu, F., Jankowiak, I., and Smirnov, A.: AERONET—A federated instrument network and data archive for aerosol characterization. Remote Sensing of Environment, 66, 1–17, https://doi.org/10.1016/S0034-4257(98)00031-5, 1998.

Holben, B. N., Kim, J., Sano, I., Mukai, S., Eck, T. F., Giles, D. M., Schafer, J. S., Sinyuk, A., Slutsker, I., Smirnov, A., Sorokin, M., Anderson, B. E., Che, H., Choi, M., Crawford, J. H., Ferrare, R. A., Garay, M. J., Jeong, U., Kim, M., Kim, W., Knox, N., Li, Z., Lim, H. S., Liu, Y., Maring, H., Nakata, M., Pickering, K. E., Piketh, S., Redemann, J., Reid, J. S., Salinas, S., Seo, S., Tan, F., Tripathi, S. N., Toon, O. B., and Xiao, Q.: An overview of mesoscale aerosol processes, comparisons, and validation studies from DRAGON networks, Atmos. Chem. Phys., 18, 655–671, https://doi.org/10.5194/acp-18-655-2018, 2018.

Hsu, N. C., Lee, J., Sayer, A. M., Kim, W., Bettenhausen, C., and Tsay, S.-C.: VIIRS deep blue aerosol products over land: extending the EOS long-term aerosol data records, J. Geophys. Res.-Atmos., 124, 7, 4026–4053, https://doi.org/10.1029/2018JD029688, 2019.

Ingmann, P., Veihelmann, B., Langen, J., Lamarre, D., Stark, H., and Courreges-Lacoste, G. B.: Requirements for the GMES atmosphere service and ESA's implementation concept: Sentinels-4/5 and -5p. Remote Sensing of Environment, 120, 58–69. https://doi.org/10.1016/j.rse.2012.01.023, 2012.

IPCC: Climate Change 2013: The Physical Science Basis. Contribution of Working Group I to the Fifth Assessment Report of the Intergovernmental Panel on Climate Change, edited by: Stocker, T. F., Qin, D., Plattner, G.-K., Tignor, M., Allen, S. K., Boschung, J., Nauels, A., Xia, Y., Bex, V., and Midgley, P. M., Cambridge University Press, Cambridge, United Kingdom and New York, NY, USA, 1535 pp., 2013.

975

Itahashi S., Uno I., Irie H., Kurokawa JI., Ohara T.: Impacts of Biomass Burning Emissions on Tropospheric NO_2 Vertical Column Density over Continental Southeast Asia. In: Vadrevu K., Ohara T., Justice C. (eds) Land-Atmospheric Research Applications in South and Southeast Asia. Springer Remote Sensing/Photogrammetry. Springer, Cham. https://doi.org/10.1007/978-3-319-67474-2_4, 2018.

980

Jefferson, A., Hageman, D., Morrow, H., Mei, F., and Watson, T.: Seven years of aerosol scattering hygroscopic growth measurements from SGP: Factors influencing water uptake, J. Geophys. Res.-Atmos., 122, 17, 9451–9466, https://doi.org/10.1002/2017JD026804, 2017.

985 Jena, C., Ghude, S. D., Pfister, G. G., Chate, D. M., Kumar, R., Beig, G., Surendran, D. E., Fadnavis, S., and Lal, D.M.: Influence of springtime biomass burning in South Asia on regional ozone (O_3): A model based case study, Atmos. Environ., 100, 37–47, http://dx.doi.org/10.1016/j.atmosenv.2014.10.027, 2015.

Jeong, U., Kim, J., Ahn, C., Torres, O., Liu, X., Bhartia, P. K., Spurr, R. J. D., Haffner, D., Chance, K., and Holben, B. N.: An optimal-estimation-based aerosol retrieval algorithm using OMI near-UV observations, Atmos. Chem. Phys., 16, 177–193, https://doi.org/10.5194/acp-16-177-2016, 2016.

Jeong, U., Tsay, S.-C., Pantina, P., Butler, J. J., Loftus, A. M., Abuhassan, N., Herman, J. R., Dimov, A., Holben, B. N., and Swap, R. J.: Langley calibration analysis of solar spectroradiometric measurements: Spectral aerosol optical thickness retrievals, J. Geophys. Res. Atmos., 123, 4221–4238, https://doi.org/10.1002/2017JD028262, 2018.

Jeong, U., Tsay, S.-C., Giles, D. M., Holben, B. N., Swap, R. J., Abuhassan, N., and Herman, J. R.: The SMART-s Trace Gas and Aerosol Inversions: I. Algorithm Theoretical Basis for Column Property Retrievals, J. Geophys. Res. Atmos., 125, 7, e2019JD32088, https://doi.org/10.1029/2019JD032088, 2020.

1000

Jeong, U., Tsay, S.-C., Puppala, S. P., Bhujel, A., Welton, E. J., Panday, A. K., Holben, B. N., Hsu, N. C.: Spatiotemporal variabilities of aerosols and trace gases over Southern slope of Himalayan mountains during the High Mountain Asia campaign, *to be submitted to Aerosol Air Qual. Res.*, 2022.

1005 Jethva, H. and Torres, O.: Satellite-based evidence of wavelength-dependent aerosol absorption in biomass burning smoke inferred from Ozone Monitoring Instrument, Atmos. Chem. Phys., 11, 10541–10551, https://doi.org/10.5194/acp-11-10541-2011, 2011.

Khodmanee, S., and Amnuaylojaroen, T.: Impact of Biomass Burning on Ozone, Carbon Monoxide, and Nitrogen Dioxide in 1010 Northern Thailand, Front. Environ. Sci. 9, 641877, https://doi.org/10.3389/fenvs.2021.641877, 2021.

Kim, H., Barkey, B., and Paulson, S. E.: Real refractive indices of α- and β-pinene and toluene secondary organic aerosols generated from ozonolysis and photo-oxidation, J. Geophys. Res., 115, D24212, https://doi.org/10.1029/2010JD014549, 2010.

1015 Kim, J.; Jeong, U.; Ahn, M.-H.; Kim, J.H.; Park, R.J.; Lee, H.; Song, C.H.; Choi, Y.-S.; Lee, K.-H.; Yoo, J.-M.; et al.: New Era of Air Quality Monitoring from Space: Geostationary Environment Monitoring Spectrometer (GEMS), Bull. Am. Meteor. Soc. 101, E1–E22, https://doi.org/10.1175/bams-d-18-0013.1, 2020.

Kinne, S., Ackerman, T. P., Shiobara, M., Uchiyama, A., Heymsfield, A. J., Miloshevich, L., Wendell, J., Eloranta, E. W., 1020 Purgold, C., and Bergstrom, R. W.: Cirrus cloud radiative and microphysical properties from ground observations and in situ measurements during FIRE 1991 and their application to exhibit problems in cirrus solar radiative transfer modelling, J. Atmos. Sci., 54, 2320–2344, https://doi.org/10.1175/1520-0469(1997)054<2320:CCRAMP>2.0.CO;2, 1997.

Konovalov, I. B., Beekmann, M., Berezin, E. V., Formenti, P., and Andreae, M. O.: Probing into the aging dynamics of biomass 1025 burning aerosol by using satellite measurements of aerosol optical depth and carbon monoxide, Atmos. Chem. Phys., 17, 4513–4537, https://doi.org/10.5194/acp-17-4513-2017, 2017.

Koop, T., Bookhold, J., Shiraiwa, M., and Pöschl, U.: Glass transition and phase state of organic compounds: dependency on molecular properties and implications for secondary organic aerosols in the atmosphere, Phys. Chem. Chem. Phys., 13, 19238–1030 19255, https://doi.org/10.1039/C1CP22617G, 2011.

Korkin, S., Lyapustin, A., Sinyuk, A., Holben, B. N., and Kokhanovsky, A.: Vector radiative transfer code SORD: Performance analysis and quick start guide, J. Quant. Spectrosc. Ra., 200, 295-310, https://doi.org/10.1016/j.jqsrt.2017.04.035, 2017.

1035 Krotkov, N., Bhartia, P. K., Herman, J., Slusser, J., Scott, G., Labow, G., Vasilkov, A. P., Eck, T. F., Dubovik, O., and Holben, B. N.: Aerosol ultraviolet absorption experiment (2002 to 2004), part2: absorption optical thickness, refractive index, and single scattering albedo, Opt. Eng., 44, 041005, https://doi.org/10.1117/1.1886819, 2005a.

Krotkov, N., Herman, J. J., Cede, A., and Labow, G.: Partitioning between aerosol and NO_2 absorption in the UVA, in: Ultraviolet Ground- and Space-based Measurements, Models, and Effects V, edited by: Bernhard, G., Slusser, J. R., Herman, J. R., and Gao, W., Proceedings of SPIE, 5886, Bellingham, WA, 588601, 2005b.

Laskin, A., Laskin, J., and Nizkorodov, A.: Chemistry of atmospheric brown carbon, Chem. Rev., 115, 4335–4382, https://doi.org/10.1021/cr5006167, 2015.

Lee, J., Hsu, N. C., Sayer, A. M., Seftor, C. J., and Kim, W. V.: Aerosol layer height with enhanced spectral coverage achieved by synergy between VIIRS and OMPS-NM measurements, IEEE Geoscience and Remote Sensing Letters, 18, 6, https://doi.org/10.1109/LGRS.2020.2992099, 2021.

Levy, R. C., Mattoo, S., Munchak, L. A., Remer, L. A., Sayer, A. M., Patadia, F., and Hsu, N. C.: The collection 6 MODIS aerosol products over land and ocean, Atmos. Meas. Tech., 6, 2989–3034, https://doi.org/10.5194/amt-6-2989-2013, 2013.

Li, L., Dubovik, O., Derimian, Y., Schuster, G. L., Lapyonok, T., Litvinov, P., Ducos, F., Fuertes, D., Chen, C., Li, Z., Lopatin, A., Torres, B., and Che, H.: Retrieval of aerosol components directly from satellite and ground-based measurements, Atmos. Chem. Phys., 19, 13409–13443, http://doi.org/10.5194/acp-19-13409-2019, 2019.

Lin, N.-H., Tsay, S.-C., Maring, H. B., Yen, M.-C., Sheu, G.-R., Wang, S.-H., Chi, K. H., Chuang, M.-T., Ou-Yang, C.-F., Fu, J. S., Reid, J. S., Lee, C.-T., Wang, L.-C., Wang, J.-L., Hsu, C. N., Sayer, A. M., Holben, B. N., Chu, Y.-C., Nguyen, X. A., Sopajaree, K., Chen, S.-J., Cheng, M.-T., Tsuang, B.-J., Tsai, C.-J., Peng, C.-M., Schnell, R. C., Conway, T., Chang, C.-T., Lin, K.-S., Tsai, Y. I., Lee, W.-J., Chang, S.-C., Liu, J.-J., Chiang, W.-L., Huang, S.-J., Lin, T.-H., and Liu, G.-R.: An overview of regional experiments on biomass burning aerosols and related pollutants in Southeast Asia: From BASE-ASIA and the Dongsha Experiment to 7-SEAS, Atmos. Environ., 78, 1–19, http://dx.doi.org/10.1016/j.atmosenv.2013.04.066, 2013.

Liu, P., Zhang, Y., and Martin, S. T.: Complex refractive indices of thin films of secondary organic materials by spectroscopic ellipsometry from 220 to 1200 nm, Environ. Sci. Technol., 47, 13594−13601, https://dx.doi.org/10.1021/es403411e, 2013.

Mie, G.: Beiträge zur Optik trüber Medien, speziell kolloidaler Metallösungen, Annalen der Physik. 330, 3, 377–445, https://doi.org/10.1002/andp.19083300302, 1908.

Mishchenko, M. I., Geogdzhayev, I. V., Liu, L., Ogren, J. A., Lacis, A. A., Rossow, W. B., Hovenier, J. W., Volten, H., and Munoz, O.: Aerosol retrievals from AVHRR radiances: effects of particle nonsphericity and absorption and an updated long-

term global climatology of aerosol properties, J. Quant. Spectrosc. Ra., 79, 953–972, https://doi.org/10.1016/S0022-4073(02)00331-X, 2003.

1075   Mok, J., Krotkov, N. A., Torres, O., Jethva, H., Li, Z., Kim, J., Koo, J.-H., Go, S., Irie, H., Labow, G., Eck, T. F., Holben, B. N., Herman, J., Loughman, R. P., Spinei, E., Lee, S. S., Khatri, P., and Campanelli, M.: Comparisons of spectral aerosol single scattering albedo in Seoul, South Korea, Atmos. Meas. Tech., 11, 2295–2311, https://doi.org/10.5194/amt-11-2295-2018, 2018.

1080   Moosmüller, H., Chakrabarty, R.K., Arnott, W.P.: Aerosol light absorption and its measurement: A review, J. Quant. Spectrosc. Ra., 110, 844–878, http://doi.org/10.1016/j.jqsrt.2009.02.035, 2009.

Müller, T., Schladitz, A., Kandler, K., and Wiedensohler, A.: Spherical particle absorption coefficients, single scattering albedos and imaginary parts of refractive indices from ground based in situ measurements at Cape Verde Island during 1085   SAMUM-2, Tellus, 63B, 573–588, https//doi.org/10.1111/j.1600-0889.2011.00572.x, 2011.

Müller, M., Gebetsberger, M., Tiefengraber, M., and Cede, A.: Fiducial Reference Measurements for Air Quality: Calibration Procedures Document (LuftBlick_FRM4AQ_CPD_RP_2019003_v4.0), Issue 4, available at https://www.pandonia-global-network.org, 2020.

1090

Myhre, G., Samset, B. H., Schulz, M., Balkanski, Y., Bauer, S., Berntsen, T. K., Bian, H., Bellouin, N., Chin, M., Diehl, T., Easter, R. C., Feichter, J., Ghan, S. J., Hauglustaine, D., Iversen, T., Kinne, S., Kirkevåg, A., Lamarque, J.-F., Lin, G., Liu, X., Lund, M. T., Luo, G., Ma, X., van Noije, T., Penner, J. E., Rasch, P. J., Ruiz, A., Seland, Ø., Skeie, R. B., Stier, P., Takemura, T., Tsigaridis, K., Wang, P., Wang, Z., Xu, L., Yu, H., Yu, F., Yoon, J.-H., Zhang, K., Zhang, H., and Zhou, C.: Radiative 1095   forcing of the direct aerosol effect from AeroCom Phase II simulations, Atmos. Chem. Phys., 13, 1853–1877, https://doi.org/10.5194/acp-13-1853-2013, 2013.

Nakajima, T., Yoon, S.-C., Ramanathan, V., Shi, G.-Y., Takemura, T., Higurashi, A. Takamura, T., Aoki, K., Sohn, B.-J., Kim, S.-W., Tsuruta, H., Sugimoto, N., Shimizu, A., Tanimoto, H., Sawa, Y., Lin, N.-H., Lee, C.-T., Goto, D., and Schutgens, 1100   N.: Overview of the atmospheric brown cloud East Asian regional experiment 2005 and a study of the aerosol direct radiative forcing in east Asia, J. Geophys. Res., 112, D24S91, https://doi.org/10.1029/2007JD009009, 2007.

Nakajima, T., Campanelli, M., Che, H., Estellés, V., Irie, H., Kim, S.-W., Kim, J., Liu, D., Nishizawa, T., Pandithurai, G., Soni, V. K., Thana, B., Tugjsurn, N.-U., Aoki, K., Go, S., Hashimoto, M., Higurashi, A., Kazadzis, S., Khatri, P., Kouremeti, 1105   N., Kudo, R., Marenco, F., Momoi, M., Ningombam, S. S., Ryder, C. L., Uchiyama, A., and Yamazaki, A.: An overview of

34

and issues with sky radiometer technology and SKYNET, Atmos. Meas. Tech., 13, 4195–4218, https://doi.org/10.5194/amt-13-4195-2020, 2020.

Natraj V., Liu, X., Kulawik, S.S., Chance, K., Chatfield, R., Edwards, D. P., Eldering, A., Francis, G., Kurosu, T., Pickering, K., Spurr, R., Worden, H.: Multispectral sensitivity studies for the retrieval of tropospheric and lowermost tropospheric ozone from simulated clear sky GEO-CAPE measurements, Atmos. Environ., 45, 7151–7165. https://doi.org/10.1016/j.atmosenv.2011.09.014, 2011.

Pantina, P., Tsay, S.-C., Hsiao, T.-C., Loftus, A. M., Kuo, F., Ou-Yang, C.-F., Sayer, A. M., Wang, S.-H., Lin, N.-H., Hsu, N. C., Janjai, S., Chantara, S., and Nguyen, A. X.: COMMIT in 7-SEAS/BASELInE: Operation of and Observations from a Novel, Mobile Laboratory for Measuring In-Situ Properties of Aerosols and Gases, Aerosol Air Qual. Res., 26, 2728–2741, https://doi.org/10.4209/aaqr.2015.11.0630, 2016.

Petters, J. L., Saxena, V. K., Slusser, J. R., Wenny, B. N., and Madronich, S.: Aerosol single scattering albedo retrieved from measurements of surface UV irradiance and a radiative transfer model, J. Geophys. Res., 108, D9, 4288, https://doi.org/10.1029/2002JD002360, 2003

Petters, M. D., Carrico, C. M., Kreidenweis, S. M., Prenni, A. J., DeMott, P. J., Collett Jr. J. L., and Moosmüller, H.: Cloud condensation nucleation activity of biomass burning aerosol, J. Geophys. Res., 114, D22205, https://doi.org/10.1029/2009JD012353, 2009

Pistone, K., Redemann, J., Doherty, S., Zuidema, P., Burton, S., Cairns, B., Cochrane, S., Ferrare, R., Flynn, C., Freitag, S., Howell, S. G., Kacenelenbogen, M., LeBlanc, S., Liu, X., Schmidt, K. S., Sedlacek III, A. J., Segal-Rozenhaimer, M., Shinozuka1, Y., Stamnes, S., van Diedenhoven, B., Van Harten, G., and Xu, F.: Intercomparison of biomass burning aerosol optical properties from in situ and remote-sensing instruments in ORACLES-2016, Atmos. Chem. Phys., 19, 9181–9208, https://doi.org/10.5194/acp-19-9181-2019, 2019.

Reid, J. S., Eck, T. F., Christopher, S. A., Hobbs, P. V., and B. N. Holben: Use of the Ångström exponent to estimate the variability of optical and physical properties of aging smoke particles in Brazil, J. Geophys. Res., 104, 27473–27489, https://doi.org/10.1029/1999JD900833, 1999.

Reid, J. S., Hyer, E. J., Johnson, R. S., Holben, B. N., Yokelson, R. J., Zhang, J., Campbell, J. R., Christopher, S. A., Di Girolamo, L., Giglio, L., Holz, R. E., Kearney, C., Miettinen, J., Reid, E. A., Turk, F. J., Wang, J., Xian, P., Zhao, G., Balasubramanian, R., Chew, B. N., Janjai, S., Lagrosas, N., Lestari, P., Lin, N.-H., Mahmud, M., Nguyen, A. X., Norris, B.,

Oanh, N. T. K., Oo, M., Salinas, S. V., Welton, E. J. and Liew, S.C.: Observing and understanding the Southeast Asian aerosol system by remote sensing: An initial review and analysis for the Seven Southeast Asian Studies (7SEAS) program, Atmos. Res., 122, 403–468, https://doi.org/10.1016/jatmosres.2012.06.005, 2013.

Randerson, J. T., Chen, Y., van der Werf, G. R., Rogers, B. M., and Morton, D. C.: Global burned area and biomass burning emissions from small fires, J. Geophys. Res., 117, G04012, https://doi.org/10.1029/2012JG002128, 2012.

Rodgers, C. D.: Characterization and error analysis of profiles retrieved from remote sounding measurements. Journal of Geophysical Research, 95, 5587–5595. https://doi.org/10.1029/JD095id05p05587, 1990.

Rodgers, C. D.: Inverse method for atmospheric sounding: Theory and practice, World Scientific Publishing co. Singapore: Pte. Ltd., 2000.

Sayer, A. M., Hsu, N. C., Eck, T. F., Smirnov, A., and Holben, B. N.: AERONET-based models of smoke-dominated aerosol near source regions and transported over oceans, and implications for satellite retrievals of aerosol optical depth, Atmos. Chem. Phys., 14, 11493–11523, https://doi.org/10.5194/acp-14-11493-2014, 2014.

Schafer, J. S., Eck, T. F., Holben, B. N., Thornhill, K. L., Ziemba, L. D., Sawamura, P., Moore, R. H., Slutsker, I., Anderson, B. E., Sinyuk, A., Giles, D. M., Smirnov, A., Beyersdorf, A. J., and Winstead, E. L.: Intercomparison of aerosol volume size distributions derived from AERONET ground-based remote sensing and LARGE in situ aircraft profiles during the 2011–2014 DRAGON and DISCOVER-AQ experiments, Atmos. Meas. Tech., 12, 5289–5301, https://doi.org/10.5194/amt-12-5289-2019, 2019

Shepherd, R. H., King, M. D., Marks, A. A., Brough, N., and Ward, A. D.: Determination of the refractive index of insoluble organic extracts from atmospheric aerosol over the visible wavelength range using optical tweezers, Atmos. Chem. Phys., 18, 5235–5252, https://doi.org/10.5194/acp-18-5235-2018, 2018.

Shiraiwa, M., Ammann, M., Koop, T., and Pöschl, U.: Gas uptake and chemical aging of semisolid organic aerosol particles, Proc. Natl. Acad. Sci., 108, 27, 11003–11008, https://doi.org/10.1073/pnas.1103045108, 2011.

Sinyuk, A., Holben, B. N., Eck, T. F., Giles, D. M., Slutsker, I., Korkin, S., Schafer, J. S., Smirnov, A., Sorokin, M., and Lyapustin, A.: The AERONET Version 3 aerosol retrieval algorithm, associated uncertainties and comparisons to Version 2, Atmos. Meas. Tech., 13, 3375–3411, https://doi.org/10.5194/amt-13-3375-2020, 2020.

Spurr, R. J. D.: VLIDORT: A linearized pseudo-spherical vector discrete ordinate radiative transfer code for forward model
and retrieval studies in multilayer multiple scattering media. J. Quant. Spectrosc. Ra., 102(2), 316–342.
https://doi.org/10.1016/j.jqsrt.2006.05.005, 2006

Spurr, R. J. D., and Christi, M.: On the generation of atmospheric property Jacobians from the (V)LIDORT linearized radiative
transfer models, J. Quant. Spectrosc. Ra., 142, 109–115, https://doi.org/10.1016/j.jqsrt.2014.03.011, 2014.

Spurr, R. J. D., Wang, J., Zeng, J., and Mishchenko, M. I.: Linearized T-matrix and Mie scattering computations, J. Quant.
Spectrosc. Ra., 113, 425–439, https://doi.org/10.1016/j.jqsrt.2011.11.014, 2012.

Stamnes, K., Tsay, S.-C., Wiscombe, W., and Jayaweera, K.: Numerically stable algorithm for discrete-ordinate-method
radiative transfer in multiple scattering and emitting layered media, Appl. Opt., 27, 12, 2502–2509,
https://doi.org/10.1364/AO.27.002502, 1988.

Sumlin, B. J., Heinson, Y. W., Shetty, N., Pandey, A., Pattison, R. S., Baker, S., Hao, W. M., Chakrabarty, R. K.: UV–Vis–
IR spectral complex refractive indices and optical properties of brown carbon aerosol from biomass burning, J. Quant.
Spectrosc. Ra., 206, 392–398, https://doi.org/10.1016/j.jqsrt.2017.12.009, 2018.

Tang, M., Cziczo, D. J., and Grassian, V. H.: Interactions of water with mineral dust aerosol: water adsorption, hygroscopicity,
cloud condensation, and ice nucleation, Chem. Rev., 116, 7, 4205–4259, https://doi.org/10.1021/acs.chemrev.5b00529, 2016.

Takemura, T., Nakajima, T., Dobovik, O., Holben, B. N., and Kinne, S.: Single-scattering albedo and radiative forcing of
various aerosol species with a global three-dimensional model, J. Climate., 15, 4, 333–352, https://doi.org/10.1175/1520-
0442(2002)015<0333:SSAARF>2.0.CO;2, 2002.

Tao, J. C., Zhao, C. S., Ma, N., and Liu, P. F.: The impact of aerosol hygroscopic growth on the single-scattering albedo and
its application on the NO_2 photolysis rate coefficient, Atmos. Chem. Phys., 14, 12055–12067, https://doi.org/10.5194/acp-14-
12055-2014, 2014.

Taylor, T. E., L'Ecuyer, T. S., Slusser, J. R., Stephens, G. L., and Goering, C. D.: An operational retrieval algorithm for
determining aerosol optical properties in the ultraviolet, J. Geophys. Res., 113, D03201,
https://doi.org/10.1029/2007JD008661, 2008.

Torres, O., Ahn, C., and Chen, Z.: Improvements to the OMI near-UV aerosol algorithm using A-train CALIOP and AIRS observations, Atmos. Meas. Tech., 6, 3257–3270, https://doi.org/10.5194/amt-6-3257-2013, 2013.

1210 Tsay, S.-C., Hsu, N. C., Lau, W. K.-M., Li, C., Gabriel, P. M., Ji, Q., Holben, B. N., Welton, E. J., Nguyen, A. X., Janjai, S., Lin, N.-H., Reid, J. S., Boonjawat, J., Howell, S. G., Huebert, B. J., Fu, J. S., Hansell, R. A., Sayer, A. M., Gautam, R., Wang, S.-H., Goodloe, C. S., Miko, L. R., Shu, P. K., Loftus, A. M., Huang, J., Kim, J. Y., Jeong, M.-J., and Pantina, P.: From BASE-ASIA toward 7-SEAS: A satellite-surface perspective of boreal spring biomass-burning aerosols and clouds in Southeast Asia, Atmos. Environ., 78, 20–34, http://dx.doi.org/10.1016/j.atmosenv.2012.12.013, 2013.

1215

Tsay, S.-C., Maring, H. B., Lin, N.-H., Buntoung, S., Chantara, S., Chuang, H.-C., Gabriel, P. M., Goodlo, C. S., Holben, B. N., Hsiao, T.-C., Hsu, N. C., Janjai, S., Lau, W. K. M., Lee, C.-T., Lee, J., Loftus, A. M., Nguyen, A. X., Nguyen, C. M., Pani, S. K., Pantina, P., Sayer, A. M., Tao, W.-K., Wang, S.-H., Welton, E. J., Wiriya, W., and Yen, M.-C.: Satellite-Surface Perspectives of Air Quality and Aerosol-Cloud Effects on the Environment: An Overview of 7-SEAS/BASELInE, Aerosol

1220 Air Qual. Res., 16, 2581–2602, https://doi.org/10.4209/aaqr.2016.08.0350, 2016.

Uchiyama, A., Matsunaga, T., and Yamazaki, A.: The instrument constant of sky radiometers (POM-02) – Part 1: Calibration constant, Atmos. Meas. Tech., 11, 5363–5388, https://doi.org/10.5194/amt-11-5363-2018, 2018a.

1225 Uchiyama, A., Matsunaga, T., and Yamazaki, A.: The instrument constant of sky radiometers (POM-02) – Part 2: Solid view angle, Atmos. Meas. Tech., 11, 5389–5402, https://doi.org/10.5194/amt-11-5389-2018, 2018b.

Valenzuela, A., Reid, J. P., Bzdek, B. R., and Orr-Ewing A. J.: Accuracy required in measurements of refractive index and hygroscopic response to reduce uncertainties in estimates of aerosol radiative forcing efficiency, J. Geophys. Res. Atmos.,

1230 123, 6469–6486, https://doi.org/10.1029/2018JD028365, 2018.

Wetzel, M. A., Shaw, G. E., Slusser, J. R., Borys, R. D., and Cahill, C. F.: Physical, chemical, and ultraviolet radiative characteristics of aerosol in central Alaska, J. Geophys. Res., 108, 4418, https://doi.org/10.1029/2002JD003208, 2003.

1235 Womack, C. C., Manfred, K. M., Wagner, N. L., Adler, G., Franchin, A., Lamb, K. D., Middlebrook, A. M., Schwarz, J. P., Brock, C. A., Brown, S. S., and Washenfelder, R. A.: Complex refractive indices in the ultraviolet and visible spectral region for highly absorbing non-spherical biomass burning aerosol, Atmos. Chem. Phys., 21, 7235–7252, https://doi.org/10.5194/acp-21-7235-2021, 2021.

1240   Wu, Z., Chen, J., Wang, Y., Zhu, Y., Liu, Y., Yao, B., Zhang, Y., and Hu, M.: Interactions between water vapor and atmospheric aerosols have key roles in air quality and climate change, Natl. Sci. Rev., 5, 4, 452–454, https://doi.org/10.1093/nsr/nwy063, 2018.

Xu, W., Han, T., Du, W., Wang, Q., Chen, C., Zhao, J., Zhang, Y., Li, J., Fu, P., Wang, Z., Worsnop, D. R., and Sun, Y.:
1245   Effects of Aqueous-Phase and Photochemical Processing on Secondary Organic Aerosol Formation and Evolution in Beijing, China, Environ. Sci. Technol., 51, 762−770, https://doi.org/10.1021/acs.est.6b04498, 2017

Yang, P., Feng, Q., Hong, G., Kattawar, G. W., Wiscombe, W. J., Mishchenko, M. I., Dubovik, O., Laszlo, I., and Sokolik, I. N.: Modeling of the scattering and radiative properties of nonspherical dust-like aerosols, J. Aerosol Sci., 38, 995–1014.
1250   https://doi.org/10.1016/j.jaerosci.2007.07.001, 2007.

Yu, H., Kaufman, Y. J., Chin, M., Feingold, G., Remer, L. A., Anderson, T. L., Balkanski, Y., Bellouin, N., Boucher, O., Christopher, S., DeCola, P., Kahn, R., Koch, D., Loeb, N., Reddy, M. S., Schulz, M., Takemura, T., and Zhou, M.: A review of measurement-based assessments of the aerosol direct radiative effect and forcing, Atmos. Chem. Phys., 6, 613–666,
1255   https://doi.org/10.5194/acp-6-613-2006, 2006.

Table 1: Examples of reported real part refractive index of biomass burning and dust aerosols from previous and current study.

Reference	Aerosol type	Wavelengths	Real part of the refractive index
Kim et al. (2010)	Secondary organic aerosols	670 nm	1.38 – 1.61
Liu et al. (2013)	Secondary organic aerosols	220 – 1200 nm	1.48 – 1.58
Sheperd et al. (2018)	Urban, remote, wood smoke	460 – 760 nm	~1.58 for wood smoke aerosols 1.47 – 1.52 for urban and remote aerosols
Sumlin et al. (2018)	Brown carbon aerosols	375 nm, 405 nm, 532 nm, 1047 nm	1.5 – 1.7
Biagio et al. (2019)	Dust aerosols	370 nm, 470 nm, 520 nm, 590 nm, 660 nm, 880 nm, 950 nm	1.48 – 1.55
Womack et al. (2021)	Biomass burning	360 – 720 nm	1.55 – 1.6
This study	Major fraction of biomass-burning aerosols mixed with minor fraction of dust particles	330 – 780 nm	1.53 ± 0.03 for fine mode 1.51 ± 0.02 for coarse mode

1260

Table A1: Relative azimuth angles, wavelength node, sources of measurement error covariance matrix, and parameters of state vector of SMART–s algorithm.

Algorithm parameter	Description
Relative azimuth angles	3.0°, 3.5°, 4.0°, 5.0°, 6.0°, 7.0°, 8.0°, 10.0°, 12.0°, 14.0°, 16.0°, 18.0°, 20.0°, 25.0°, 30.0°, 35.0°, 40.0°, 45.0°, 50.0°, 60.0°, 70.0°, 80.0°, 90.0°, 100.0°, 120.0°, 140.0°, 160.0°, and 180.0°
Wavelength node	330 nm, 340 nm, 350 nm, 360 nm, 370 nm, 380 nm, 390 nm, 400 nm, 410 nm, 440 nm, 455 nm, 490 nm, 520 nm, 540 nm, 555 nm, 580 nm, 610 nm, 640 nm, 675 nm, 750 nm, and 778 nm
Sources of measurement error covariance matrix	Estimated from Langley and laboratory calibration results
State vector	Lognormal parameters of aerosol number-size distribution for fine- and coarse-mode, number-fine-mode fraction, two parameters of gaussian vertical profile shape of aerosols, spectral complex refractive indices of fine- and coarse-mode, spectral surface reflectance

1265
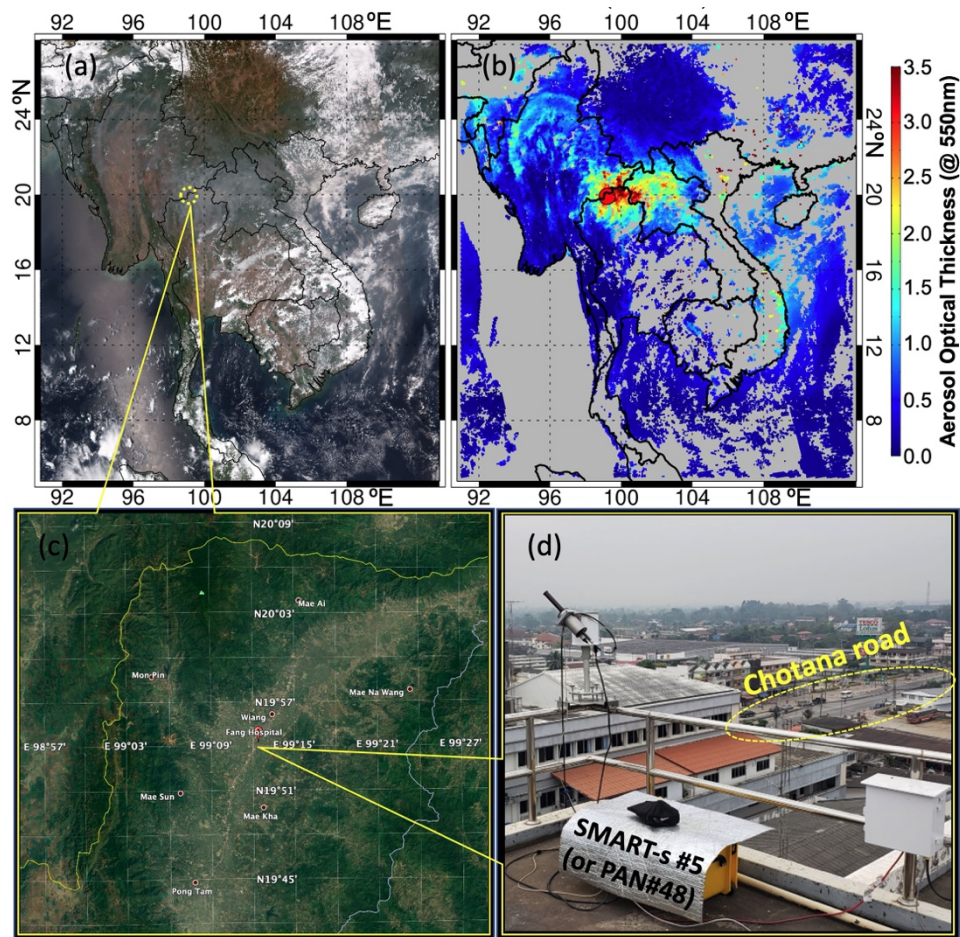
Figure 1: (a) True color image and **(b)** DB (Deep Blue) τ_{aer} product from VIIRS (Visible Infrared Imaging Radiometer Suite) onboard SNPP (Suomi National Polar-orbiting Partnership) on 30 March 2019. Yellow circle in panel (a) is the location of Fang, Thailand, and colored circle of panel (b) shows collocated τ_{aer} retrievals from the SMART–s. Panel (c) indicates the location of measurement site at the rooftop of Fang hospital, Thailand (19.91°N latitude and 99.21°E longitude, 480 m above sea level; the map is extracted from https://google.com/maps/; © Google Maps 2021). Panel (d) is an image of deployed SMART–s (Pandora#48) taken on 8 March 2019. The Chotana road (marked in yellow) is one of the major streets at this area and is about 50 m away from the site.

41
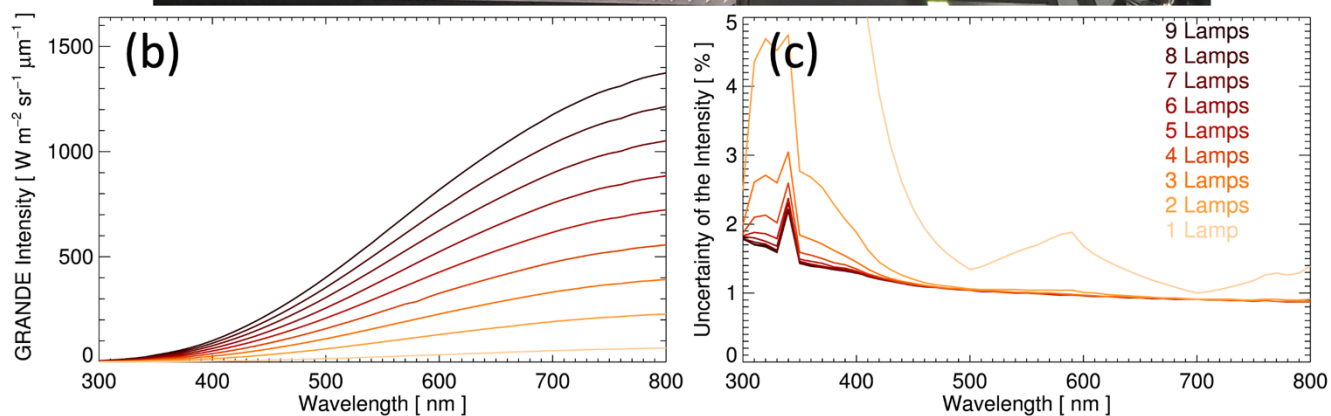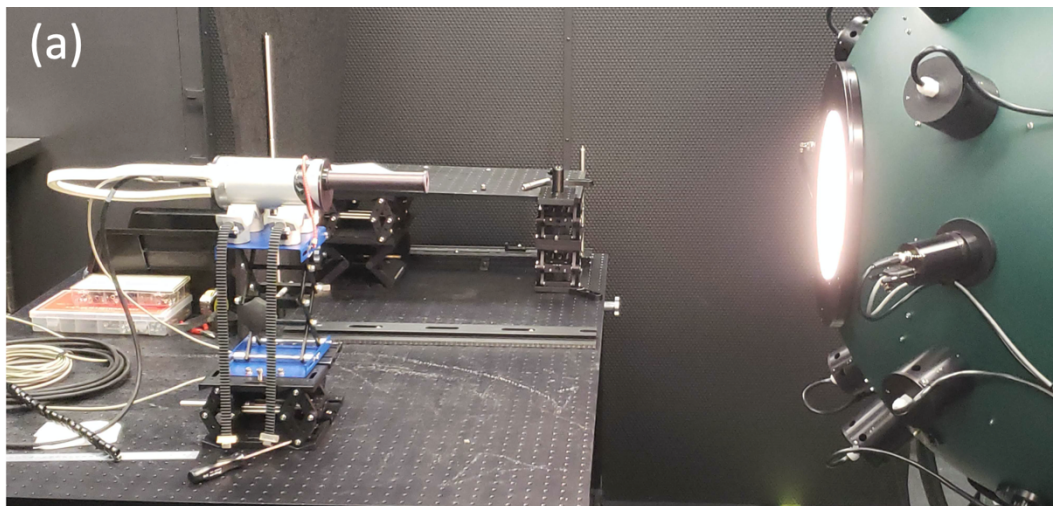
Figure 2: (a) Image of SMART–s calibration using the NIST-traceable light source (Grande) at the Radiometric Calibration Laboratory, NASA Goddard Space Flight Center. Panel (b) shows spectral radiance of the Grande in 300 − 800 nm, and panel (c) presents its reported uncertainty. Different colors in (b) and (c) indicate nine levels of the Grande radiance. The relatively higher values of uncertainty near 350 nm in panel (c) are due to filter change of sensor during the light-source calibration.

1280
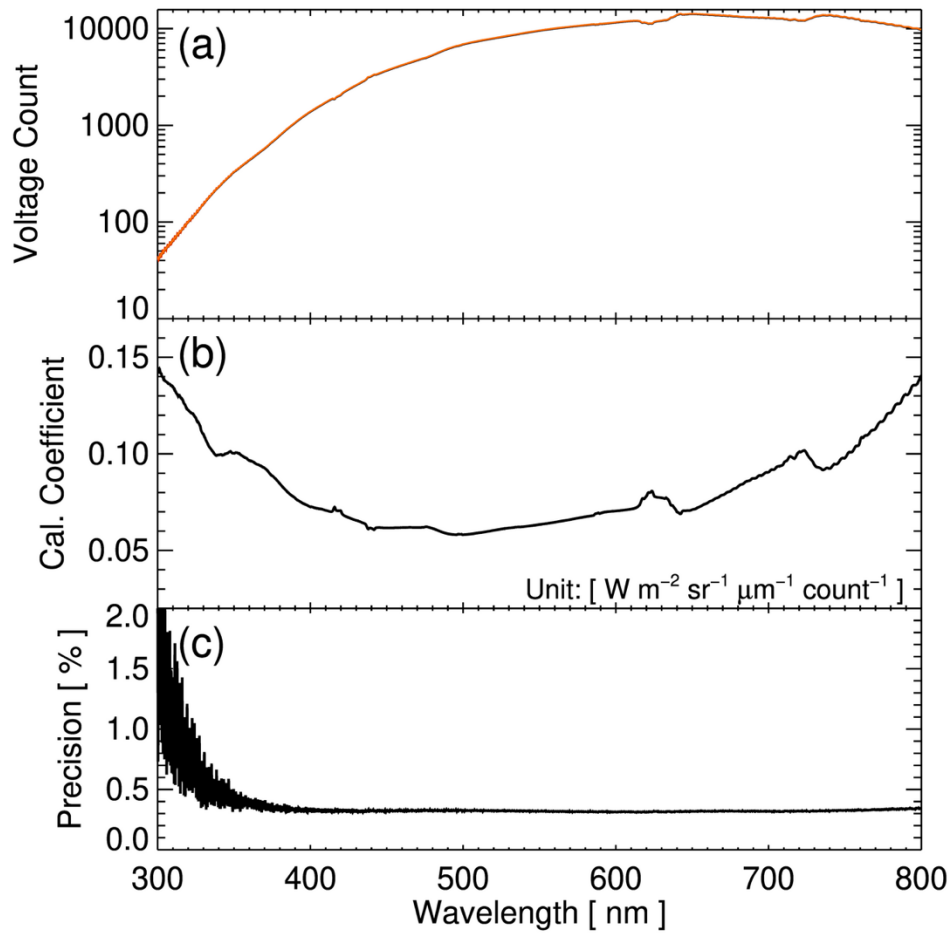
Figure 3: (a) An example of nine-lamps Grande voltage count measurements from SMART–s (Pandora#48) without neutral density or band-pass filters. Different colors indicate ten times of repetitions, which overlap almost on top of each other. Panel (b) is calibration coefficient, which is calculated from dividing known Grande intensity by average value of the measured voltage count. (c) is precision of the calibration coefficient, which is estimated by calculating one standard deviation of the ten times of repetitions.
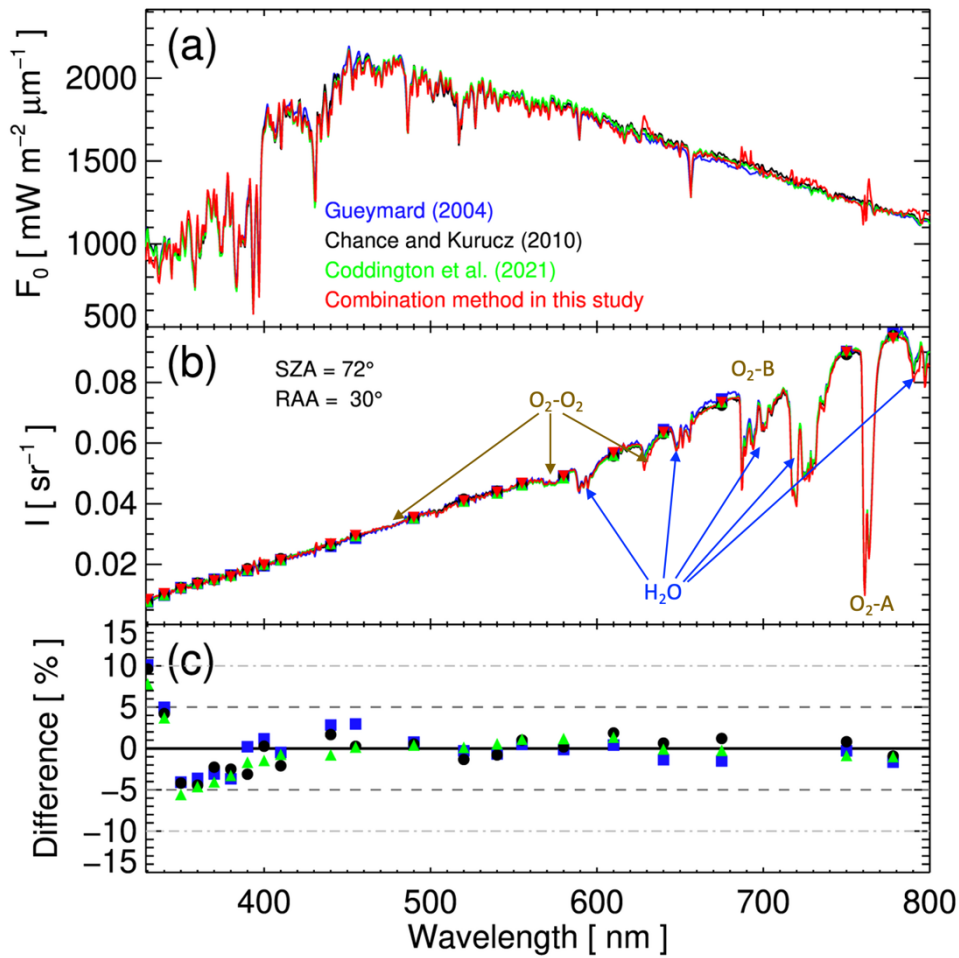
Figure 4: (a) Spectral solar irradiances (F_0) from Gueymard, 2004 (blue), Chance and Kurucz, 2010 (black), Coddington et al., 2021 (green), and combination method developed in this study (F_{Comb} in red). Panel (b) is an example of converted normalized radiance (radiance divided by solar irradiance, F_0) measured at Fang, Thailand on 19 March 2019. Colored lines indicate different sources of F_0 for the conversion (same as in panel-a), and circles, triangles, and rectangles depict selected wavelengths of aerosol inversion in this study. Panel (c) presents relative biases of the F_{Comb} compared to those of Gueymard, 2004 (blue rectangle), Chance and Kurucz, 2010 (black circle), and Coddington et al.,2021 (green triangle).
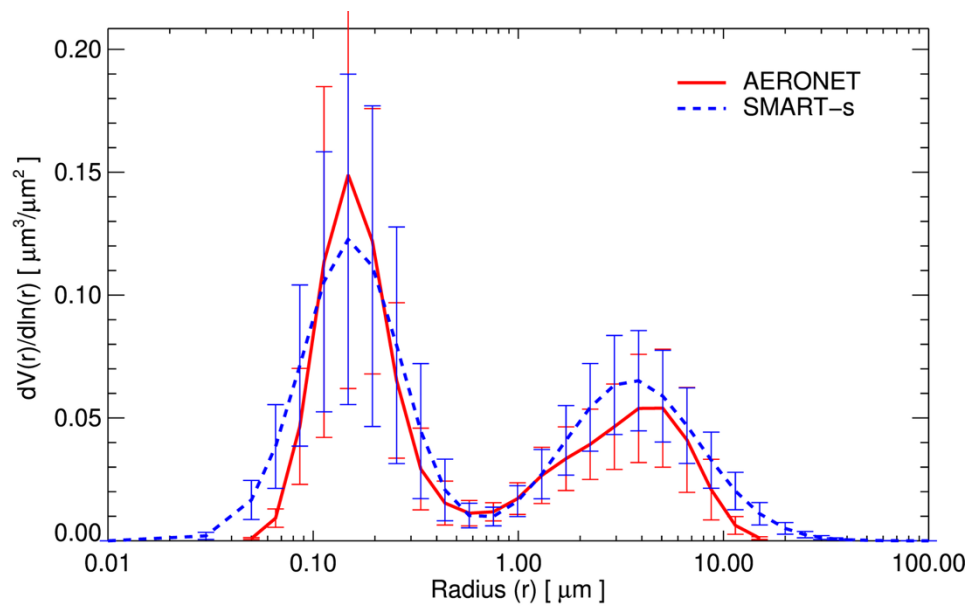
1295

Figure 5: Average volume-size-distribution of aerosols retrieved from SMART–s (blue dashed line) and AERONET (red solid line) from 19 March to 2 May 2019 at Fang, Thailand. Standard deviations at each radius node during the period are represented as vertical bars in this figure. The SMART–s spectral range is not sensitive to aerosols with radius greater than about 10 μm, and the SMART–s retrievals over this range (see long tails of the blue dashed-line) are mostly determined by the lognormal-shape
1300 **assumption.**
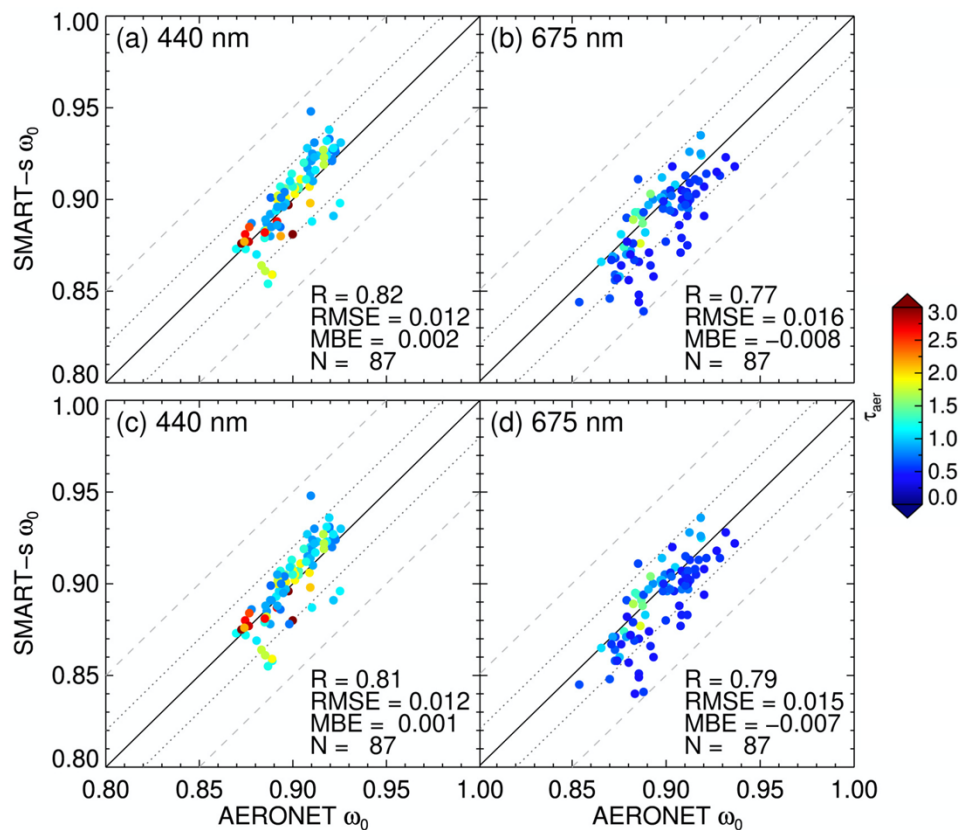
Figure 6: Comparison of single-scattering albedo (ω_0) from SMART–s and AERONET (Version 3, Level 2.0) at (a) 440 nm and (b) 675 nm from 19 March to 2 May 2019. In these two panels, SMART–s algorithm utilized solar irradiance from Coddington et al. (2021). Panels (c) and (d) are similar plots to (a) and (b) but for SMART–s retrievals using derived solar irradiance in this study. Colored circles represent values of aerosol optical thickness (τ_{aer}) from the colorbar at each wavelength. The R is the correlation coefficient, RMSE denotes root-mean-square error, and MBE is the mean-bias error, and N is the number of samples for the comparison. The dotted and dashed lines represent respectively relative biases of ±0.02 and ± 0.05 from the AERONET product.
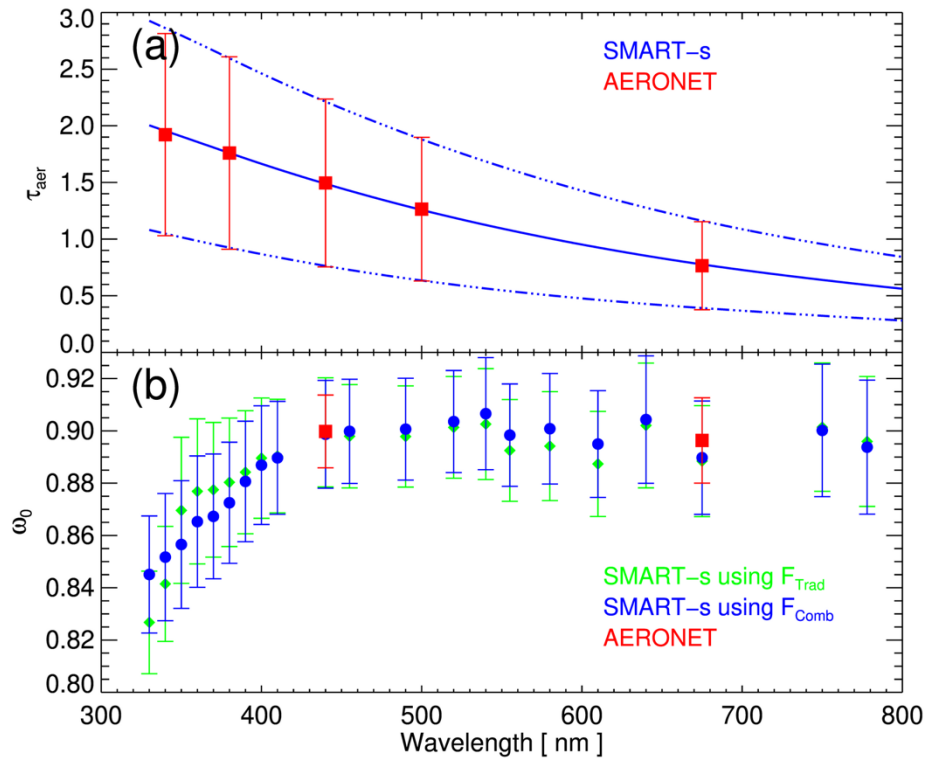
Figure 7: Mean values of (a) aerosol optical thickness (τ_{aer}) from SMART–s (blue line) and AERONET (red square) within 330–800 nm spectral range measured from 19 March to 2 May 2019 at Fang, Thailand. Panel (b) shows those of spectral single-scattering albedo of aerosols (ω_0) from AERONET (red rectangle) and SMART–s using different solar irradiance; green diamonds used that of Coddington et al. (2021) and blue circles used spectrum derived in this study. Variabilities (one standard deviations) of each value during the deployment period are shown as dashed-dotted lines in panel (a) and vertical bars in panel (a) and (b).
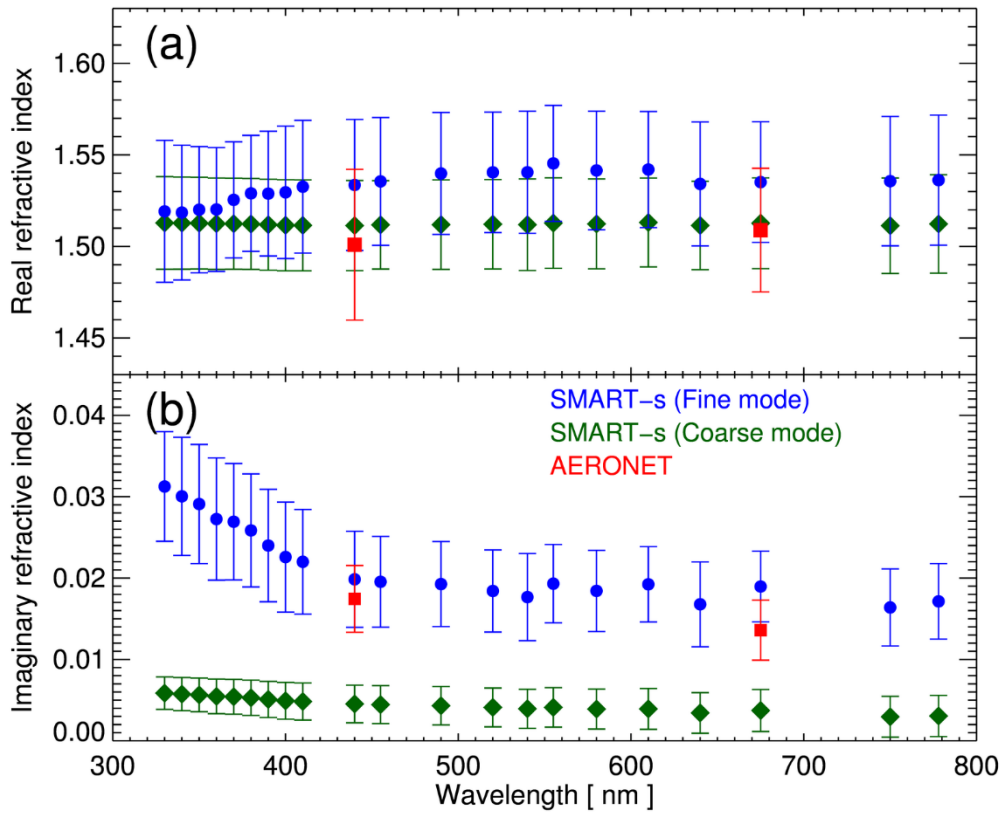
Figure 8: Mean values of (a) real part of spectral refractive index from AERONET (red square) and SMART–s (blue circle: fine-mode, green diamond: coarse-mode) within SMART–s spectral range measured from 19 March to 2 May 2019 at Fang, Thailand. Panel (b) shows those of Imaginary part. Variabilities (one standard deviations) of each value during the deployment period are demonstrated as vertical bars in panel (a) and (b).
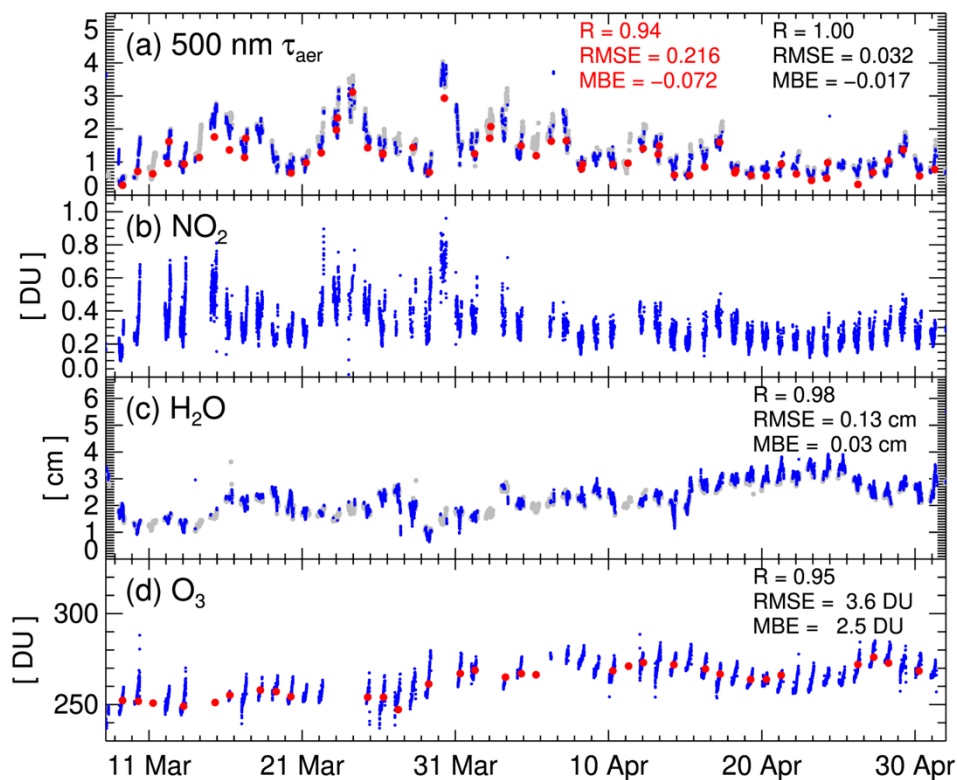
1325

Figure 9: Temporal variations of total columns of (a) aerosol extinction at 500 nm, (b) nitrogen dioxide, (c) precipitable water vapor, and (d) ozone at Fang, Thailand in 2019. The blue circles are from SMART–s retrievals, and the grey circles in panels (a) and (c) show those from the AERONET. In panel (a), the red circles indicate aerosol optical thickness at 550 nm from VIIRS Deep Blue (DB), while those in panel (d) depict total column ozone retrievals from OMI (TOMS Version 8.5). The correlation coefficient (R),

1330   root-mean-squared-error (RMSE), and mean-bias-error (MBE) at panels (a), (c), and (d) are between collocated SMART–s and AERONET/OMI data in black, and those of red color in panel (a) are between SMART–s and VIIRS DB retrievals.
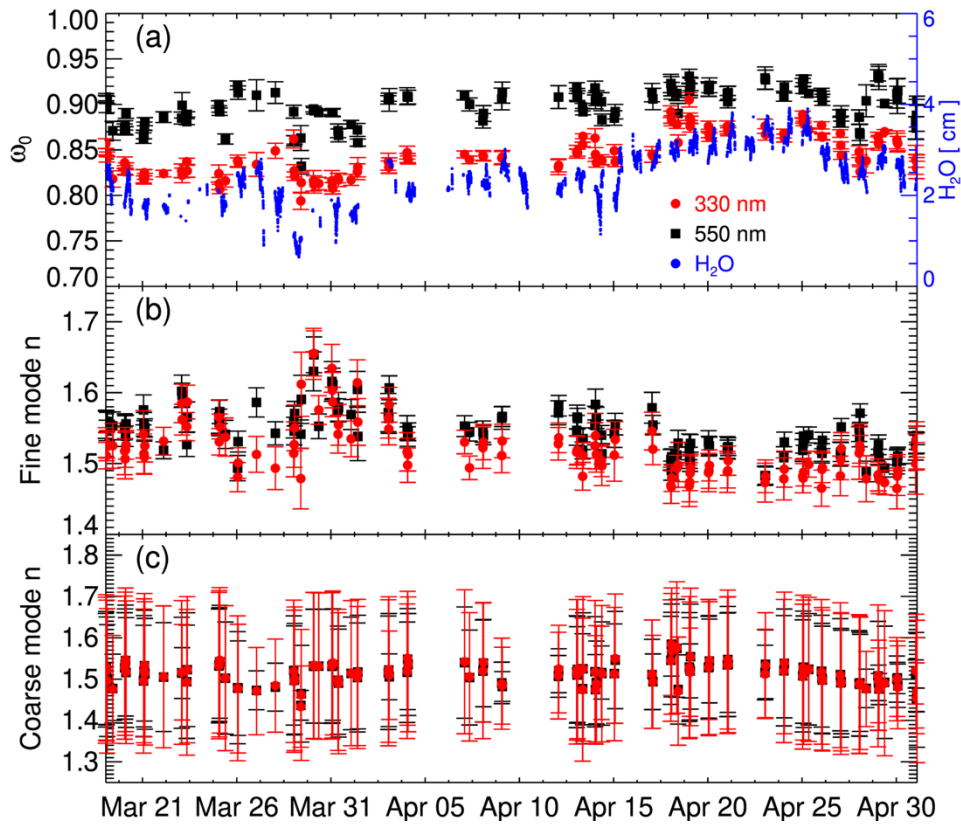
1335

Figure 10: Temporal variations of (a) total aerosol single-scattering albedo (ω_0), real-part of aerosol refractive index (*n*) of (b) fine-mode and (c) coarse-mode retrieved at Fang, Thailand in 2019. The red circles black squares indicate retrievals at 330 nm and 550 nm, respectively. The vertical bars indicate estimated errors of each retrieval based on the optimal-estimation method. The small blue circles in panel (a) represent total column H_2O retrievals from SMART–s.
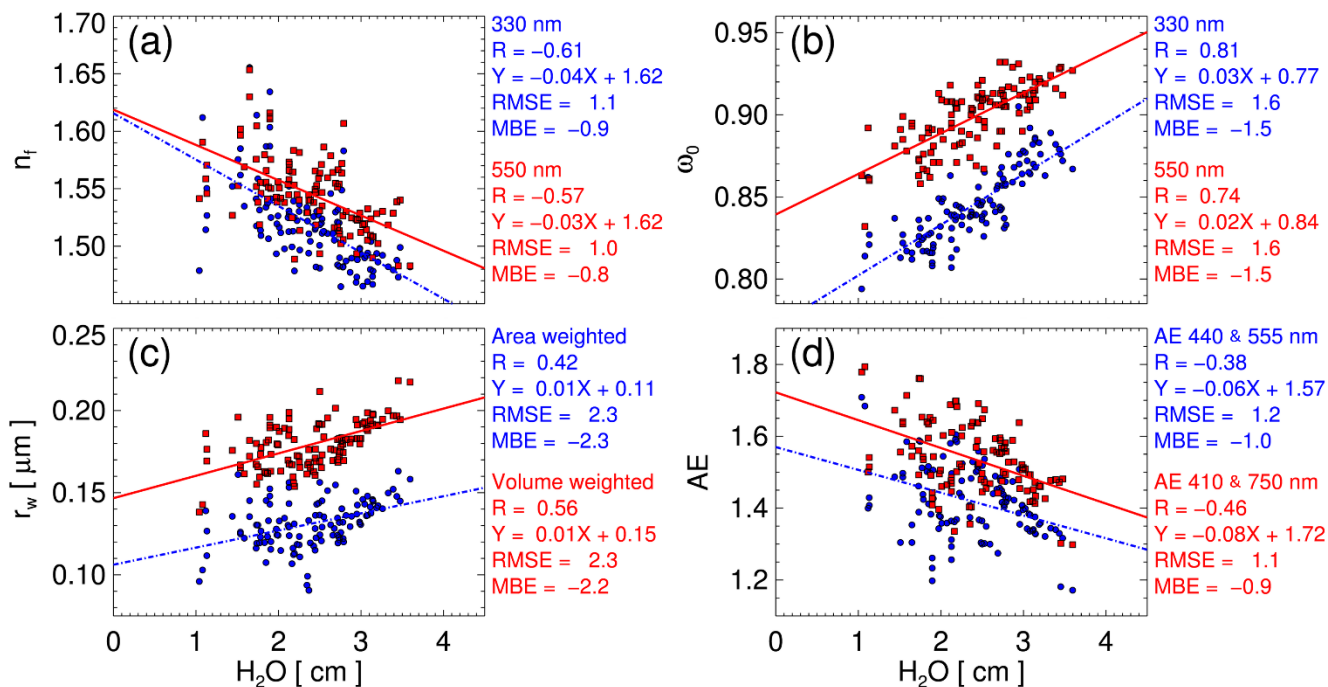
Figure 11: Relationship between aerosol properties and column precipitable H_2O retrieved from SMART−s over Fang, Thailand from 19 March to 2 May 2019. Panels (a) and (b) compare real-part of the refractive index of fine-mode (n_f), and aerosol single-scattering albedo (ω_0) to H_2O, respectively. For the upper panels, blue and red color represent n_f and ω_0 at 330 nm and 550 nm, respectively. Panels (c) and (d) compare weighted-mean-radius (r_w) and Ångström exponent (AE) to the column precipitable H_2O, respectively. The blue and red symbols in panel (c) represent area- and volume-weighted mean radius, and those in panel (d) indicate different wavelength pairs for the AE calculations (blue using 440 nm and 555 nm, and red using 410 nm and 750 nm).

51
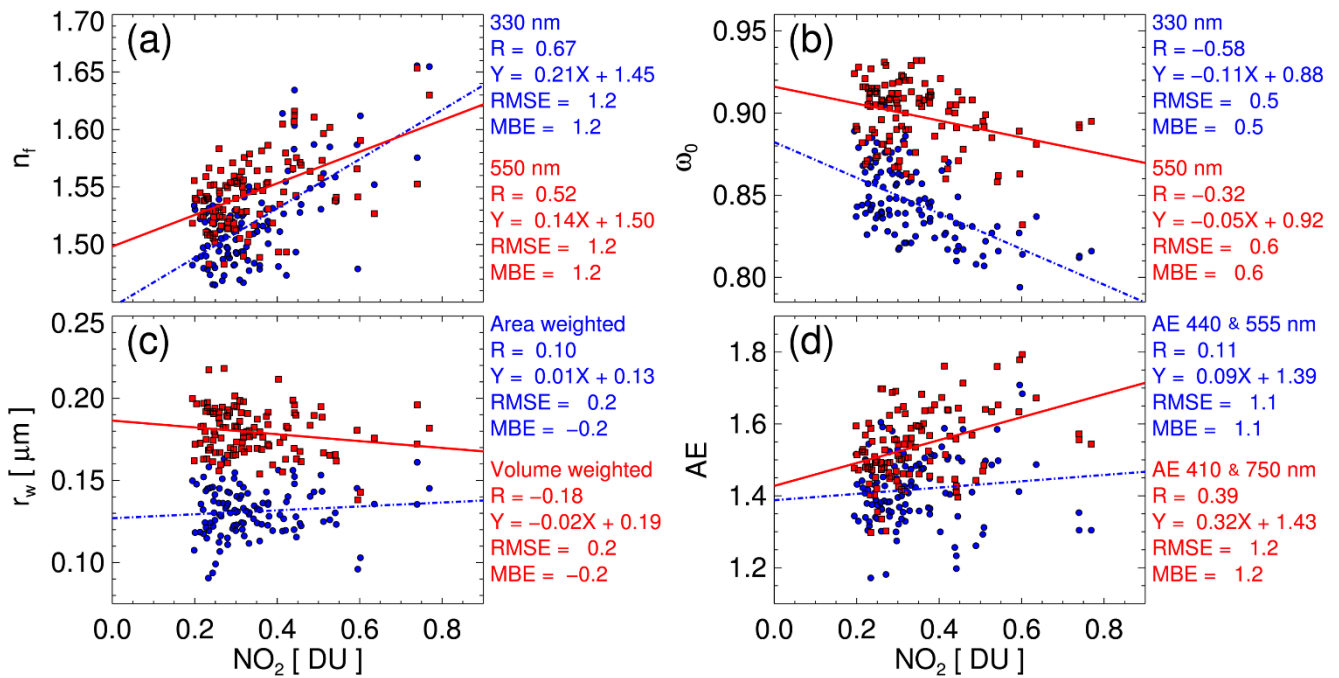
Figure 12: Comparison of total column amount of NO₂ to (a) real-part of the refractive index of fine-mode (n_f) and (b) aerosol single-scattering albedo (ω_0). The blue and red colors symbolize those retrieved at 330 nm and 550 nm, respectively. Panels (c) and (d) compare weighted-mean-radius (r_w) and Ångström exponent (AE) to the total column NO₂, respectively. The blue and red symbols in panel (c) represent area- and volume-weighted mean radius, and those in panel (d) indicate different wavelength pairs for the AE calculations (blue using 440 nm and 555 nm, and red using 410 nm and 750 nm).
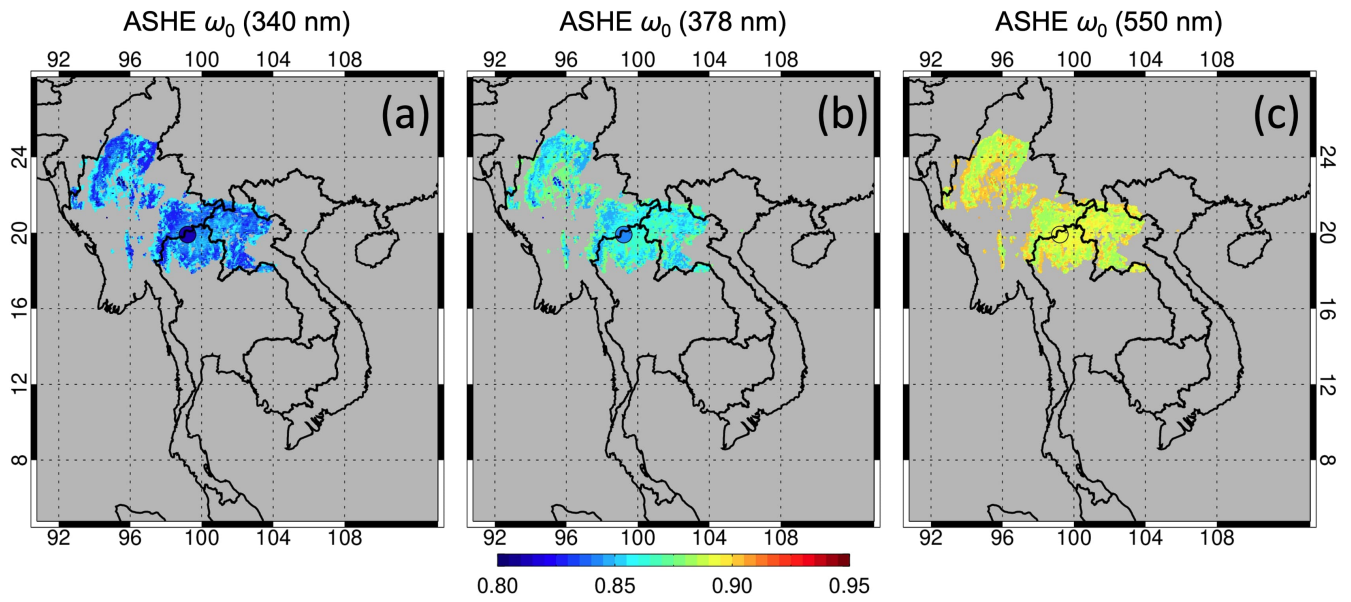
Figure 13: Aerosol single-scattering albedo (ω_0) retrieved at (a) 340 nm, (b) 378 nm and (c) 550 nm from ASHE (Aerosol Single-scattering albedo and Height Estimation; Lee et al., 2021) algorithm on 30 March 2019. Colored circles present values of collocated SMART–s retrievals indicated by the colorbar at each wavelength.
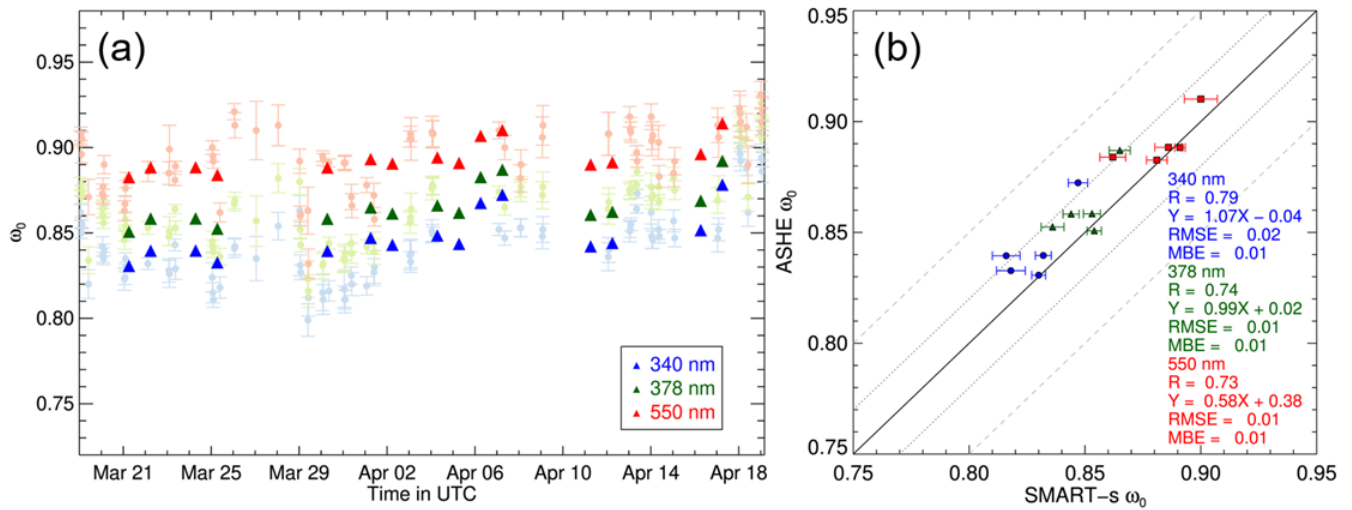
Figure 14: (a) Temporal variations of aerosol spectral single-scattering albedo (ω_0; 340 nm in blue, 378 nm in green, and 550 nm in red) retrieved from ASHE (dark colors; Aerosol Single-scattering albedo and Height Estimation; Lee et al., 2021) and SMART–s (faint colors) over Fang, Thailand in 2019. The ASHE retrievals are not available after 18 April 2019, since UVAI over the site decreased lower than the ASHE criteria likely due to the increased ω_0 over the period. Panel (b) compares retrieved ω_0 from ASHE and SMART–s at each wavelength during the period. The dotted and dashed lines represent respectively relative biases of ±0.02 and ± 0.05 from the SMART–s product. The collocated samples are limited to have a time difference less than 3 hours. The vertical and horizontal bars in panels (a) and (b), respectively, indicate estimated errors of each retrieval based on the optimal-estimation method.
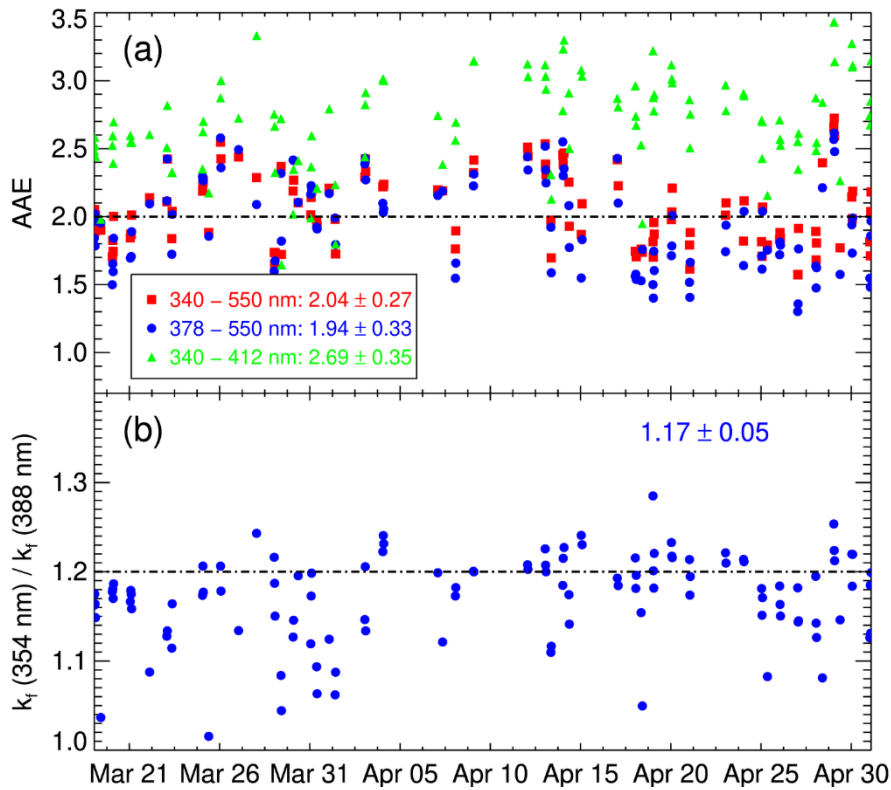
Figure 15: Temporal variations of (a) absorbing Ångström exponent (AAE) of aerosols, and (b) ratio of fine-mode imaginary refractive indices (k_f) of aerosols at 354 nm and 388 nm retrieved at Fang, Thailand in 2019. The color-coded symbols in panel (a) represent different wavelength pairs: red for 340 – 550 nm, blue for 378 – 550 nm, and green for 340 – 412 nm. The dash-dot lines in panel (a) and (b) are assumed values of ASHE and OMAERUV algorithms for smoke aerosols, respectively.
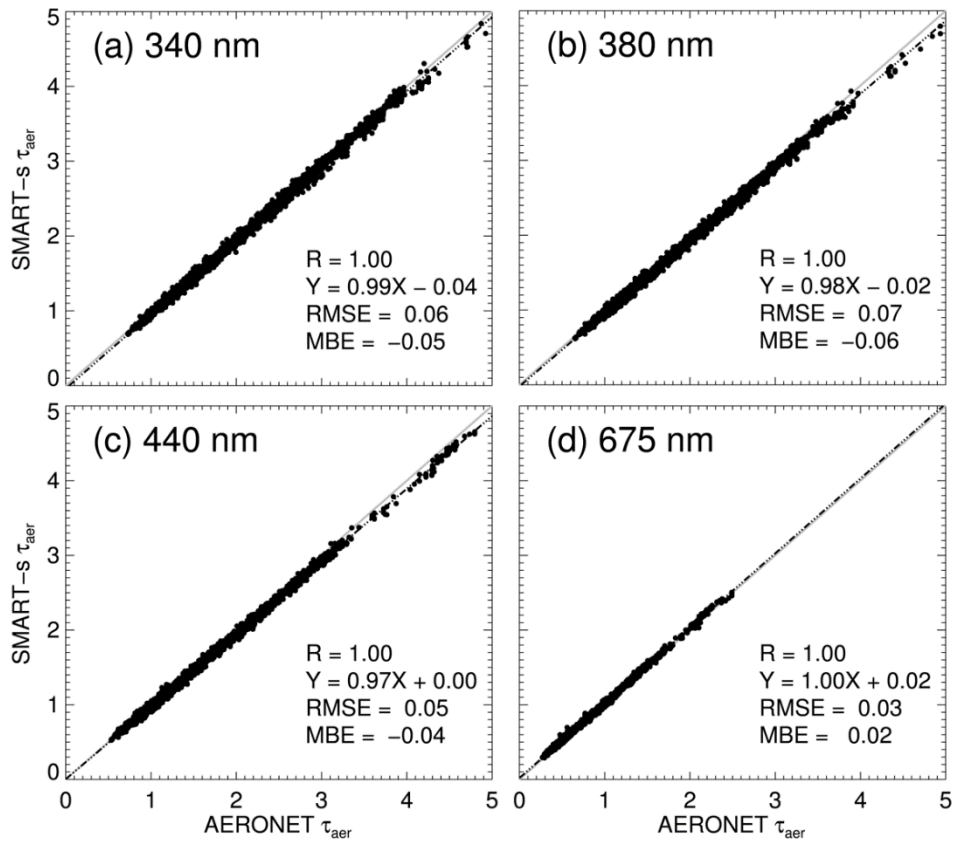
Figure A1: Comparison of aerosol optical thickness (τ_{aer}) from SMART–s and AERONET (Version 3, Level 2.0) at (a) 340 nm, (b) 380 nm, (c) 440 nm, and (d) 675 nm measured at Fang, Thailand from 8 March to 2 May in 2019. The R is the correlation coefficient, RMSE denotes root-mean-square error, and MBE is the mean-bias error. The black dot-dashed line and the grey solid line represent regression and one-to-one lines, respectively.

1380
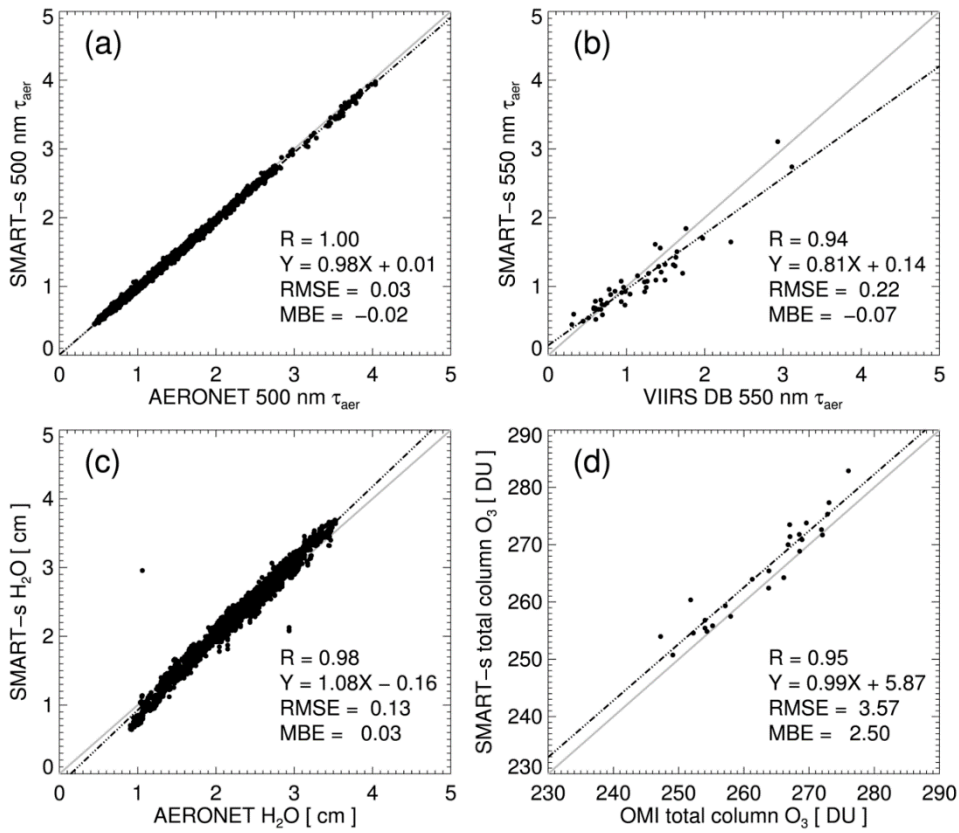
Figure A2: Panel (a) compares aerosol optical thickness (τ_{aer}) at 500 nm from SMART–s and AERONET (Version 3, Level 2.0), and (b) compares that at 550 nm from VIIRS DB and SMART–s. Total precipitable water vapor (H_2O) products from SMART–s and AERONET are compared in panel (c), and total column ozone retrievals from OMI and SMART–s are compared in panel (d). The retrievals are obtained at Fang, Thailand from 8 March to 2 May in 2019. The R is the correlation coefficient, RMSE denotes root-mean-square error, and MBE is the mean-bias error. The black dot-dashed line and the grey solid line represent regression and one-to-one line, respectively.
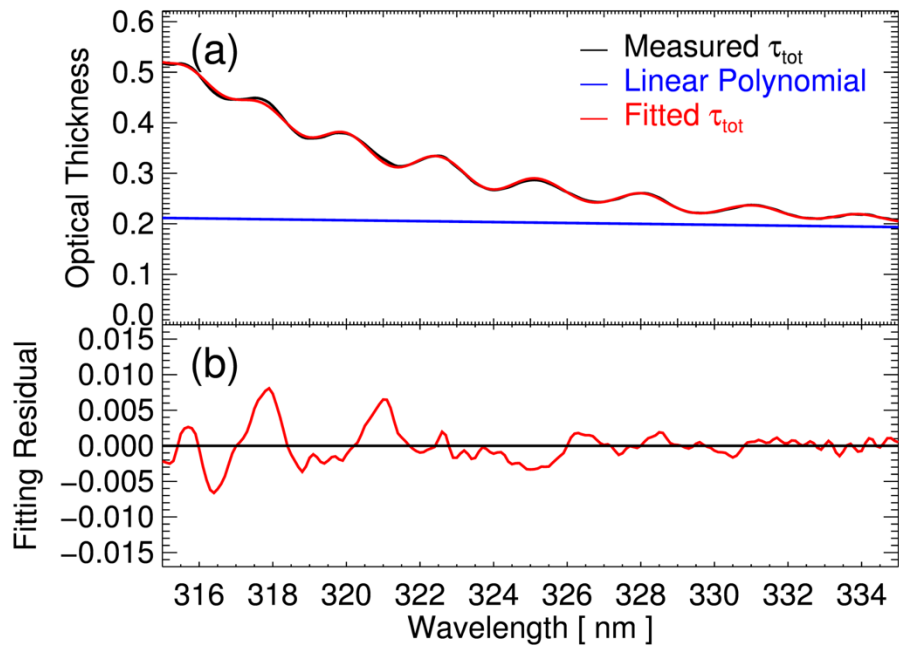
Figure A3: (a) Spectral fitting result of the SMART–s O$_3$ algorithm at 16:50 UTC on 14 October 2019 measured on the rooftop of the NASA Goddard Space Flight Center Building 33 (38.99°N latitude, 76.84°W longitude). Panel (b) presents fitting residual (measured optical thickness subtracted by model optical thickness).
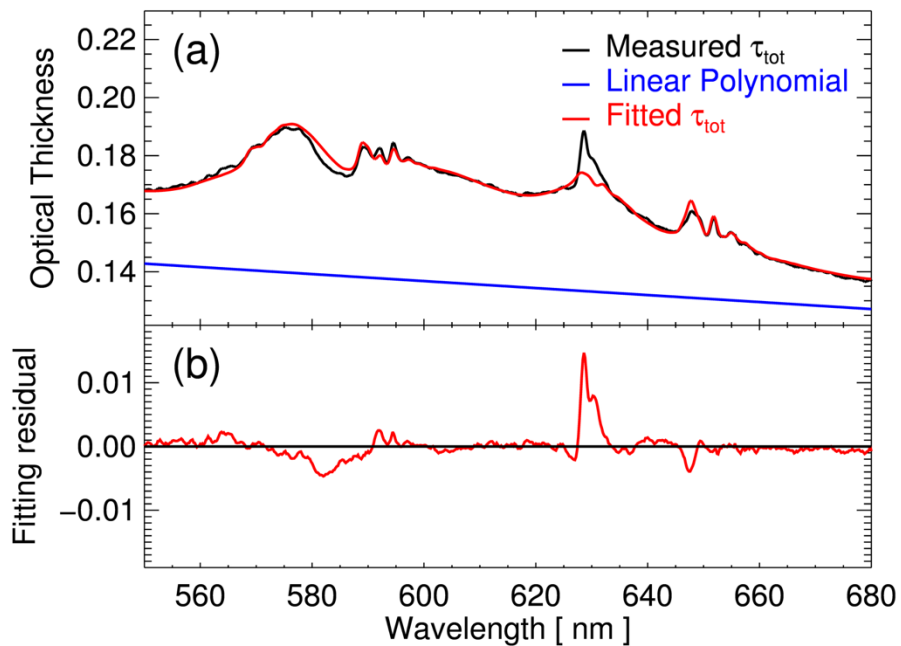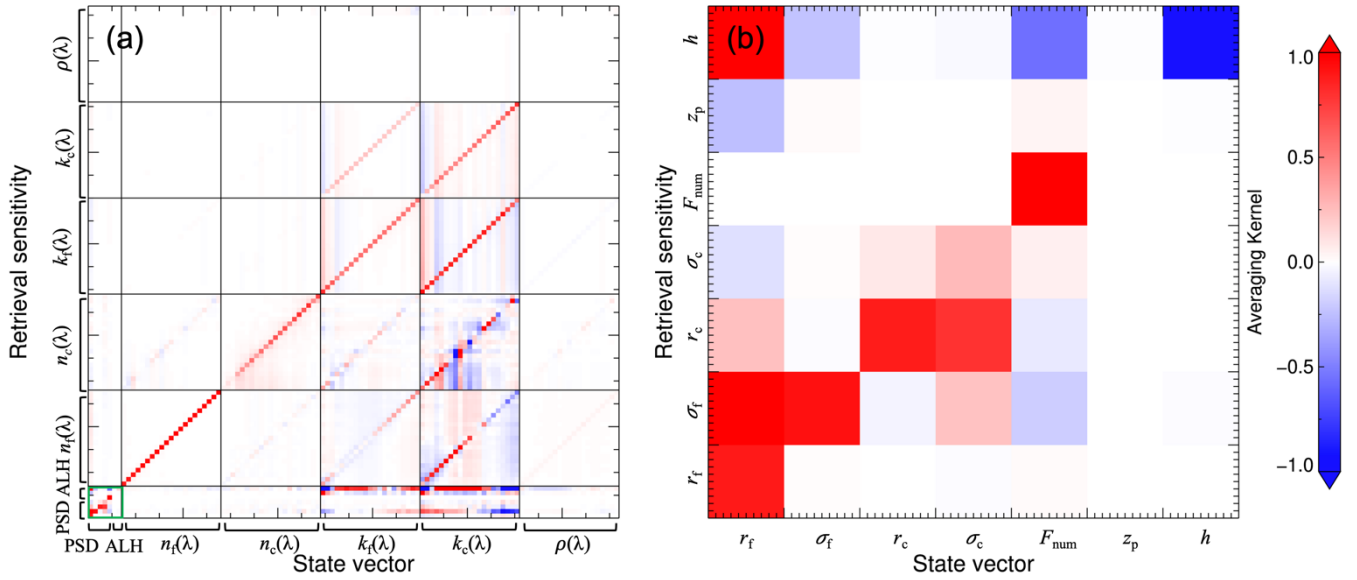
1395

Figure A4: Similar figure of Figure A3 but for H₂O; (a) Spectral fitting result of the SMART–s H₂O algorithm at 16:55 UTC on 14 October 2019 measured at the same location. Panel (b) presents fitting residual (measured optical thickness subtracted by model optical thickness).

Figure A5: Averaging kernel matrix (A) of SMART–s retrievals at 08:31 UTC on 10 April 2019 at Fang, Thailand, when fine-/coarse-mode volume fractions were comparable, and aerosol single-scattering albedo was about 0.87 with aerosol optical thickness about 1.06 at 440 nm. Indices from 1 to 5 correspond to fine-mode mean radius (r_f) and geometric standard deviation (σ_f), those pair for coarse mode (r_f and σ_f), and number fine-mode fraction (F_{num}). Indices 6 and 7 are peak height (z_p) and dispersion parameter (h) of the assumed aerosol extinction profile. Each element of real (n) and imaginary (k) part of the refractive index for fine-(subscript f) and coarse-mode (subscript c) indicates its retrieval sensitivity at each wavelength. Panel (a) shows the whole A, and panel (b) zooms to particle-size-distribution (PSD) and aerosol-layer-height (ALH) parameters (indices from 1 to 7) as indicated as a green square in panel (a).
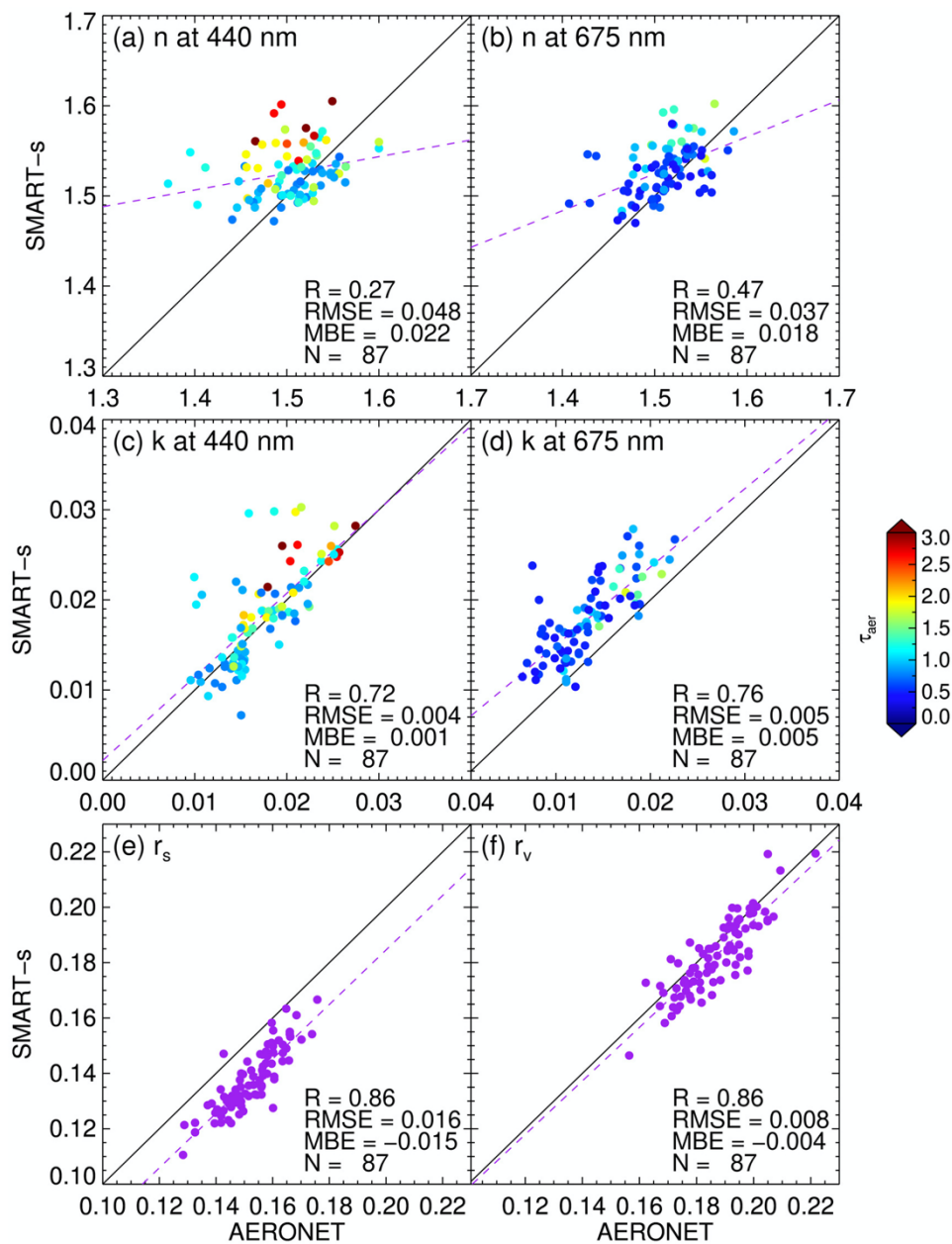
Figure A6: Comparison of aerosol inversion products from SMART–s and AERONET (Version 3, Level 2.0) from 19 March to 2 May 2019. Upper panels compare the real part of the refractive index at (a) 440 nm and (b) 675 nm, and middle panels compare the imaginary part at these wavelengths. Colored circles in panel (a)-(d) represent values of aerosol optical thickness (τ_{aer}) from the colorbar at each wavelength. Lower panels compare (e) area- and (f) volume-weighted-mean-radii (r_s and r_v, respectively). The R is the correlation coefficient, RMSE denotes root-mean-square error, and MBE is the mean-bias error, and N is the number of samples for the comparison. Black solid-line and purple dashed-line depict one-to-one and regressions, respectively.

1415

1420